DEVELOPMENT OF PROCESSING MAPS BY PHYSICAL SIMULATION OF LOW ALLOY MEDIUM CARBON STEEL

A DISSERTATION

Submitted in partial fulfilment of the

requirements for the award of the degree

of

MASTER OF TECHNOLOGY

in

DEPARTMENT OF METALLURGICAL AND MATERIALS ENGINEERING

(With specialization in Industrial Metallurgy)

BY

NIRANJAN KUMAR

DEPARTMENT OF METALLURGICAL AND MATERIALS ENGINEERING

INDIAN INSTITUTE OF TECHNOLOGY ROORKEE

ROORKEE – 247667, INDIA

MAY, 2016

INDIAN INSTITUTE OF TECHNOLOGY ROORKEE

CANDIDATE'S DECLARATION

I hereby certify that the work which is being presented in the dissertation, entitled **"DEVELOPMENT OF PROCESSING MAPS BY PHYSICAL SIMULATION OF LOW ALLOY MEDIUM CARBON STEEL "** in partial fulfilment of the requirements for the degree of **Master of Technology** in the **Department of Metallurgical and Materials Engineering** with specialization in **"Industrial Metallurgy"**, **Indian Institute of Technology Roorkee**, is an authentic record of my own work carried out during the period from May, 2015 to May, 2016 under the supervision of **Dr. S. K. Nath**, Professor, Department of Metallurgical and Materials Engineering, Indian Institute of Technology Roorkee, Roorkee.

The matter embodied in the dissertation has not been submitted to any of the University/Institute for the award of any other degree.

Date: (**NIRANJAN KUMAR**)

Place: **(14544013)**

CERTIFICATE

This is to certify that the above statement made by the candidate is correct to the best of my knowledge.

(**Dr. S. K. Nath)**

Professor

MMED, IIT Roorkee

ABSTRACT

There is leading applications and importance of steels continue in many critical areas even when the availability of ceramics, polymers, composites etc. with improved properties exists. “Nothing can replace a steel, only a steel having better property can replace the existing steel”. Low alloy medium carbon steel have very wide applications in automobile parts, railway rails, wheels, shafts, high tensile tubing, high tensile fasteners, pins, gear, connecting rods, crankshafts and many more. To produce quality products at low cost, new approach should be employed to optimize the processing parameters. Thermo-mechanical processing (TMP) is a technique that can control the hot deformation processing parameters (strain, deformation temperature and strain rate), due to which mechanical properties of material enhanced.

In this study, the hot deformation behavior of low alloy medium carbon steel is studied by hot compression tests on Gleeble® 3800 thermo-mechanical simulator. The tests were carried out in temperature ranging from 800ºC to 1050ºC and strain rate from 0.01 s^{-1} to 10 s^{-1} for total true strain of 0.7 after austenitization at 1100ºC for 2 min. To model the flow behavior of this steel, constitutive analysis were done for calculation of Zener-Hollomon parameter and prediction of flow stress. For parameter optimization of forging and determining a safe working domain, processing maps were developed based on different materials models namely dynamic materials model (DMM), modified DMM and Poletti instability criteria. The microstructure of the deformed and water quenched specimens are obtained by light optical microscopy. The stable and instability domains of the processing map are correlated with the evolved microstructure. The flow behavior in a processing domain is also correlated with its power dissipation efficiency and values of strain rate sensitivity and Z-parameter. The deformation mechanisms are identified based on stress exponent value and further verified by micrographs.

ACKNOWLEDGMENTS

Firstly, I would like to express my deep gratitude, profound indebtedness, deepest respect and heartiest thanks to my supervisor **Dr S. K. Nath** (Prof.) Department of Metallurgical and Material Engineering (MMED), Indian Institute of Technology, Roorkee for his valuable supervision and encouragement throughout the completion of my M.Tech dissertation work. His continuous suggestions and encouragement was valuable. The words are not sufficient to express my heartfelt thanks and feelings to my mentor for their valuable guidance, support and believing in me.

Now I would like to express my sincere thanks to Mr. Rajendra Sharma, Mr. R. K. Sharma for their help and support towards completion of my dissertation work. I would like to thank technical and administrative staffs of the MMED who help me in all possible ways during my M.Tech work.

I wish to thank my friends and student colleagues especially Mr. Rakesh Ahlawat, Mr. Yogendra Pratap Singh, Mr. Neeraj Kumar Prasad, Mr. Gulshan Kumar Pradhan, Mr. Vignesh S. and all the fellows who helped me directly or indirectly during my entire M.Tech work.

I am thankful to the Ph.D. scholars who helped me during my work especially Mr. Sanjeev Kumar, Mr. Sumit Kumar, Mr. Guru Prakash, Mr. Neeraj Srivastava and all other who helped me during my M.Tech work.

Finally, I am everything due to my mother and I express my heartiest gratitude to my mother Mrs. Rita Devi, and other family members for their love and blessings. Their untiring support and co-operation in every step of my life make it possible for me to reach at this stage. Above all, I want to thank the supreme power of nature, who provided me strength and patience to achieve the goal.

(NIRANJAN KUMAR)

TABLE OF CONTENTS

LIST OF FIGURES

LIST OF TABLES

SYMBOLS

Ar_3	Temperature at which Austenite to ferrite transformation starts during cooling.
Ar_1	Temperature at which austenite to ferrite + martensite transformation ends during cooling.
Ac_3	Temperature at which complete austenite forms from ferrite during heating.
Ac_1	Temperature at which austenite transformation starts from ferrite during heating.
σ	Flow stress
ε	True strain
$\dot{\varepsilon}$	Strain rate
D	Power dissipation function
dT	Adiabatic temperature rise
G	Power dissipated by plastic deformation.
J	Power dissipated due to microstructural changes during deformation.
η	Power dissipation efficiency
ξ	Instability parameter of Dynamic materials model(DMM)
k	Instability parameter of Modified Dynamic materials model(MDMM)
k_j	Instability parameter proposed by Poletti et al.
m	Strain rate sensitivity
n	Stress exponent
Q	Apparent activation energy
R	Universal gas constant
T_m	Melting point of metal
Z	Zener-Hollomon parameter

LIST OF ABBREVIATIONS

CCT	Continuous cooling transformation
CDRX	Continuous dynamic recrystallization
DIFT	Deformation induced ferrite transformation
DMM	Dynamic materials model
DRV	Dynamic Recovery
DRX	Dynamic recrystallization
HSLA	High strength low alloy
LVDT	Linear voltage differential transducer
LAMCS	Low alloy medium carbon steel
LOM	Light optical microscopy
SEM	Scanning electron microscope
SFE	Stacking fault energy
SIFT	Strain induced ferrite transformation
TMP	Thermo-mechanical processing
UTS	Ultimate tensile strength

CHAPTER 1
INTRODUCTION

The application of low- alloyed medium carbon steel is increasing continuously due to its better property of forged parts. These steels are very suitable for automobile and railway parts like shafts, shaft gears, springs, connecting rods, crankshafts, wheel hubs, railway wheels, railway rails, high tensile tubing and high tensile fasteners [1]. This variety of steel has high strength to weight ratio, high toughness and good weldability. Hence, to improve other properties of forged products, the processing parameters must be optimized [2]. A proper understanding of the microstructural evolution together with the constitutive equations describing the material flow of the steel, is therefore required. The effect of processing parameters i.e. temperature, strain and strain rate on flow behavior of material can be determined by studying the flow curves of the material under different parameter combination. Among the different metal processing stage, the bulk metal working stage has major importance due to following reasons [3]:

1. Major changes in microstructure occur and have an intense effect on the succeeding processing stages.
2. In bulk metal working stage, tonnage of material being processed, so the improvements in any processing methods provides a multiplying effect on the productivity and quality of product.

Hence, substantial effort has been made to develop new techniques for the proper designing of process and its optimization. The core objective is to obtain final products having desired microstructure and mechanical properties, without any repeatable defects. Earlier, the method used is trial and error, a very expensive and time taking method and perhaps not always lead to proper optimization. In recent times, the trial and error technique is widely switched to mathematical modeling, which is based on certain scientific principles [4]. The main objectives of mathematical and physical modeling in design and manufacturing are:

1. Optimizing the processing parameter domain.
2. Controlling the microstructure in the final product.
3. Designing optimum die shapes without any shop floor trials.
4. Reduction of manufacturing lead time.

5. Increasing productivity simultaneously with improving quality of products.
6. Decrease in reduction rate by ensuring the repeatability in manufacturing.

Numerous investigations are done for the optimization of processing parameters either by physical or mathematical modeling. Nowadays, studies have been carried out using processing maps to identify the instability and safe, efficient power dissipation domains for different forming process of the material [5].

1.1 Thermo-mechanical processing (TMP)

TMP describes the heating and shaping operations under controlled process parameters like strain, strain rate and temperature and the post deformation cooling rate by which high quality components formed. It is the grouping of two separate parts- Mechanical processing and Physical Metallurgy to develop a unified approach towards new process advancement. During thermomechanical processing, by controlling the parameters, desired phase transformation, recrystallization and precipitation like different metallurgical phenomenon occurs resulting in refinement and homogenization of the final microstructure which leads to desired mechanical property.

1.2 Hot workability

It is concerned with the extent to which a material is plastically deformed during hot forming without any occurrence of flow instability. To determine the hot deformation mechanisms and optimizing the hot workability different approaches have been employed like determination of kinetic parameters, analysis of flow stress curves and development of processing maps.

1.3 Processing maps

A processing map is the representation of the behavior of a material under certain given processing conditions, in terms of microstructural mechanisms and power dissipation efficiency, and consists of an overprinting of a power dissipation and an instability map. It is a powerful tool to identify a safe and unstable domain of process parameters and decrease the rejection rate significantly. The map is very useful for characterizing the formability, process design, optimizing the process parameters and the microstructural control of materials [5]. There are many materials models proposed for processing maps like dynamic material model (DMM) developed by Prasad et al. [6], modified dynamic materials model (MDMM) proposed by Murty and Rao [7], instability parameter proposed by Poletti et al. [8]. DMM bridges the gap between the continuum mechanics of severe plastic deformation and the development of dissipative microstructures in the material. DMM considers the effect of deformation

parameters like strain, temperature and strain rate on flow behavior of materials. The flow curves obtained after compression tests were analyzed and the results were used to develop power dissipation map and the instability map on the axes of temperature and strain rate, at a constant strain. Various instability mechanisms were found during the hot working process like flow localization, adiabatic shear band formation, dynamic strain aging, strain induced precipitation. The final products obtained as a result of these processes have very poor mechanical properties and the rejection rate is quite high [9]. Hence, the instability domains must be avoided during practical hot working process.

CHAPTER 2
LITERATURE REVIEW

In this chapter, the first section explains the hot metal forming process of low alloy steel and plain medium carbon steel. The hot deformation mechanism is discussed in the second section and the third section which reviews the different materials modeling in hot deformation. Under this section, different models like kinetic model, atomistic model, DMM etc. is reviewed. Finally, in the last sections, the methods for grain refinement during hot deformation is discussed based on the available literature.

2.1 Hot forming process

Metal forming is the process of obtaining a desired shape product by application of mechanical forces. It is assumed that the metal retains the shape when the stress drops below the yield stress (except for elastic changes). For economical production and less rejection rate, defects and flaw reduction is necessary. Hot working is done with an aim to improve ductility and to lower the flow stress. At low strain rate and high temperature, there is a long time for the accumulation of energy. Due to better mobility of grain boundary and dislocation annihilation large nucleation of recrystallized (DRX) grains takes place [10]. Therefore, ductility increases and flow stress decreases at high temperatures. Generally, hot working of metals and alloys is done above the 0.6 T_m (melting point of metal) at relatively high strain rates (10^{-1} to 10^{-3} s^{-1}) [11].

Due to the industrial revolution and increasing demand of steel products all around the world, the metal forming process has a vital role in it. The thermo-mechanical treatment and large plastic deformation leads to substantial changes in microstructure and hence the properties. Additionally, mathematical modeling, computer based programs and physical simulation can predict the flow behavior, final property and microstructure. Hence, there is need to model the flow behavior and delineate the highly efficient domains and instability regime to reduce the number of trial and error and obtain a sound product.

The next section provides the overview of available literature on hot working of low alloy medium carbon steel and low alloy steel to clearly understand the deformation mechanisms and its correlation with the microstructural evolution during hot deformation.

2.1.1 Hot working of steel

Zhang et al. [12] hot compressed the plain carbon steels (C-0.08 wt. %) between 650ºC–1000ºC at a strain rate of $1s^{-1}$, using 50% and 70 % of length reduction. After 50% compression cracks could not be observed, whereas some micro-cracks were found in the specimen deformed at 650, 700, 750 and 900 ºC after 70% of compression. The initiation of these micro-cracks was strain and temperature dependent and observed at high energy region like grain sliding boundaries. The ductility of steel is a function of deformation temperature, which decreases due to the work hardening during the deformation. The shape and size of grains changed with the metal flow.

Rastegari et al. [13] deformed the plain carbon eutectoid steel (0.82% C) in the temperature and strain rate range of 620ºC –770ºC and 0.01–10 s^{-1}, to improve its ductility by transforming fully lamellar microstructure into fine ferrite + cementite microstructure. With the aid of microstructure obtained in the instability regime, different warm working defects were observed like flow localization, lamellar-sliding, lamellar kinking etc. The processing map reveals the domain where pearlite might be transformed to a spheroidized microstructure due to rapid deformation process. The results verified the feasibility of DSX mechanism in producing nano-sized (<100 nm) or the submicron size (<350 nm) cementite particles.

Venugopal et al. [9] validated the processing maps for 304L stainless steel at temperatures in the range 600°C–1200°C. The use of industrial processing operations with their strain rate range are press forging (0.15 s^{-1}), rolling/extrusion (2 s^{-1}–5 s^{-1}) and hammer forging (100 s^{-1}) were studied. The microstructure obtained after every operation was obtained and observed that the results have excellent correlation with the domains in the processing map. Flow bands, cracks and poor surface finish were identified in the instability domains and recrystallized grains in stable domains. It proved the applicability of processing maps as a tool of process design in the steel industry.

Yang et al. [1] studied the processing maps for hot compression of low carbon bainitic steel, (29MnSiCrAlNiMo) within a temperature range of 800ºC –1100ºC and a strain rate range of 0.01 to 10 s^{-1} after austenitizing at 1200ºC for 4 min. Constitutive analysis established the relation between processing parameters and yields the value of material constants and apparent deformation activation energy at different strain. The apparent activation energy for deformation decreased with increasing strain from 460 to 267 $kJmol^{-1}$ for 0.1 to 0.8 strain. Processing maps were developed at different strains have an extended instability domain with

increasing strain. The optimum hot working domain of processing parameters was identified where fully DRX occurred and fine homogeneous grain evolved. Microstructure correlation with domains of map verified its applicability in parameter optimization and microstructural control.

Rajput et al. [14] studied the hot deformation behavior of AISI 1016 steel using Gleeble 3800 physical simulator in the temperature range 750ºC–1050ºC and strain rate ranging 0.01 to 80 s^{-1} after austenitization at 1050ºC for 5 min. The processing maps were developed based on different material model and compared their applicability with respect to the obtained microstructure. High values of power dissipation efficiency (η) and strain rate sensitivity (m) at low strain rates and high temperature resulted due to DRX of austenite and high values of η and m at low strain rates and low temperatures was due to ferrite formation and DRY of ferrite.

Venugopal and Sivaprasad [5] provided a report on processing maps and its wider applications and status of research. The flow behavior of stainless steels namely AISI 304L, 316L, 304, and 304 (as-cast) and alloy D-9 were studied in the temperature range of 600°C–1200°C and strain rate of 0.001–100 s^{-1}. The microstructural examination of products formed at different parameters combination using different industrial processes verified the predictions based on laboratory tests. The important phenomena in industrial operations which affect the final product are material flow in the die-cavity, lubricant break down, deformation cracking, and die-closure etc. which can be controlled by acoustic emission (AE) technique, which is proved to be a better method for assessing the lubricant conditions and die filling. The development of an intelligent system for process control has also been proposed.

The status report on processing maps by Prasad [15] represented the processing map as a tool for analyzing numerous industrial difficulties like processing parameter optimization, quality control of final product, and avoidance of defects. As the processing map is achieving a matured stage, expert systems and artificial neural network models required to be advanced to help engineers in designing and optimization of metal working process. FORGEX, an expert system developed for forging, is probably the first one of its kind which directly addresses the materials workability problems. To recognize the patterns of metal behavior in DRX regime and instability regime, the requirement of artificial neural network models has been discussed as they can interpret the domains of processing map without any expert [16].

2.1.2 Hot compression of low alloy medium carbon steel

Numerous studies have been carried out in past on the hot deformation behavior of medium carbon steels under specified temperature and strain rate.

Omar et al. [17] hot compressed micro-alloyed medium carbon steel (C–0.34 wt. %) between deformation temperature of 900°C–1150°C and strain rates of 0.0001–10 s^{-1}. Cyclic DRX observed at low strain rates and high temperature where flow curves have multiple peaks. At medium to high temperatures and low strain rates, the flow curves display flow softening after a peak stress and a steady state in the flow stress at higher strains. The flow behavior had been widely accepted as a result of DRX process. Different deformation mechanisms were identified based on the microstructural correlation with processing domains.

Lin et al. [18] studied the microstructural evolution during the hot deformation of 42CrMo steel. The deformation was performed between 850°C–1150°C and strain rate of 0.01–50 s^{-1} after austenitizing at 1200ºC for 5min. The influence of deformation parameters on grain size was studied and found that the average grain size increases with deformation temperature and decreases with the amount of strain and strain rate. The decrease in value of the Z-parameter leads to occurrence of DRX. Hence, the fine-grained structure in metal forming can be obtained by reducing the deformation temperature and increasing the degree of deformation at a suitable strain rate provided that the temperature must be adequate for occurrence of DRX.

Lin et al. [19] optimized the processing parameters of 42CrMo steel by modeling of flow behavior using the constitutive equation analysis. The different stages of flow curves were analyzed and apparent activation energy for different strain values were calculated. The deformation activation energy increased initially with strain and then decreased as the work hardening ends and restoration (DRX/DRV) taking place. The predicted value of flow stress using constitutive modeling were compared with the experimental results to validate the established model of forging.

Vanadium microalloyed medium carbon steel (MCS) was hot compressed in the temperature range of 850ºC–1100ºC and strain rate range of 0.001–0.5 s^{-1} to strain of 0.8 by Meysami et al. [10]. The obtained deformation data were employed to calculate hot working material constants and modeling of flow behavior with the help of three constitutive equations namely power law, exponential law and hyperbolic sine law. The correctness of the hyperbolic sine law were observed with its better correlation coefficient and fitness to experimental results.

The values of critical strain and critical stress for the initiation of DRX were obtained using θ–σ curve.

Zhao et al. [20] performed uniaxial isothermal hot deformation tests on vanadium microalloyed MCS in temperature range of 750ºC–1050ºC and strain rate range of 0.005–30 s^{-1} to strain of 0.7 and activation energy (Q) of hot deformation was calculated using constitutive equations. Based on this obtained value of Q, the rate controlling mechanisms were identified. At low strain rates, the values of Q were found closer with the austenite lattice self-diffusion activation energy which indicates that dislocation climb is rate controlling mechanism and at higher values of strain rates, high values of Q indicates cross slip as a rate controlling mechanism. Processing maps were developed based on DMM and peak efficiency and instability domains were delineated.

2.2 Deformation mechanisms

The basic advantage of hot deformation is that the large strains can be achieved with very less amount of work hardening. This happens because the hardening is well balanced by the softening mechanisms like DRX, DRV etc. These restoration mechanisms are responsible for lowering the flow stress, which causes easy deformation and also transforms the grain size and surface texture of materials. Hence a proper understanding of these hardening and softening mechanisms is required for the defect free product. The six independent deformation mechanisms are listed below which can preserve the crystallinity after the plastic deformation [21].

1. Defect less flow- Flow in the defect free crystal when stress exceeds the theoretical shear strength.
2. Deformation by dislocation glide at low temperatures.
3. Due to dislocation climb and cross slip at high temperatures-dislocation creep.
4. Diffusion of point defects through grains-Nabarro-Herring creep.
5. Diffusion of point defects through their grain boundaries- Coble creep.
6. Twinning, which results in low temperature plasticity.

Based on these deformation mechanisms Ashby developed deformation mechanism maps for many pure metals and their oxides on the axes of normalized tensile strength (σ/μ) and homologous temperature (T/T_m).

2.2.1 Strain hardening mechanisms

When the temperature of hot deformation increases from 0.1 to $0.5T_m$, movement of dislocation increases. Due to strain hardening or work hardening, this movement of dislocations is hindered and hence for a plastic deformation higher amount of stress must be applied. There are many obstacles that can hinder the dislocation motion like dislocations, grain boundaries and sub grain boundaries, solute atoms, second phase particles, formation of fine precipitates in solid solution. The dislocations pass the obstacles by either cutting through the particles or around them through their boundaries.

2.2.2 Strain softening mechanisms

In hot deformation of polycrystalline materials, the strain hardening is countered by restoration mechanisms (softening). Dynamic recrystallization (DRX) and dynamic recovery (DRV) are the main softening mechanisms. After the work hardening, the dislocation density reaches maximum and then with the increase in energy, rearrangement of these dislocations takes place which causes the annihilation of dislocations and drop in flow stress. The dislocation climb and cross slip play important role in the annihilation of dislocations [18, 19]. This recovery is seen in materials having high stacking fault energy (SFE). The flow curves having DRX must attain a peak followed by softening to a steady state. At high temperatures, number of peaks are observed before attaining a steady state, called cyclic DRX [6, 13].

2.3 Workability and deformation zones

Hot workability is defined as the degree of hot deformation achieved without any defects or undesirable effects like buckling, poor surface finish, cracks, wrinkle, laps, fracture etc. As these operations are conducted at elevated temperatures, they are called ‘bulk forming processes’. For evaluation of the workability of the material tension, compression and bend tests are extensively used. Every tests has their merits and demerits, but only uniaxial hot compression test as shown in Fig. 2.1 will be described in the following section.

The compression test is considered as a standard workability test [24] because the stress value obtained after it is close to bulk deformation process. In this test, the specimen is compressed between two flat parallel dies. The aspect ratio of the specimen should lie from 1.5–2 to avoid buckling [6]. Due to friction between specimen and dies, barreling or bulging of specimen takes place (Fig. 2.2). The area of specimen in contact with the dies remains almost stationary and are called dead metal zone (Fig. 2.2 region I). The metal just outside the dead zone experiences severe deformation (Fig. 2.2 region III). The isothermal tests at a constant strain rate with

minimum friction should be conducted to determine the resistance of the material against deformation. The friction could be minimized by proper lubrication. This test is popular due to many reasons like: small specimen size, suitable cross section for optical microscopy, high amount of strains with a range of strain rates can be applied etc.

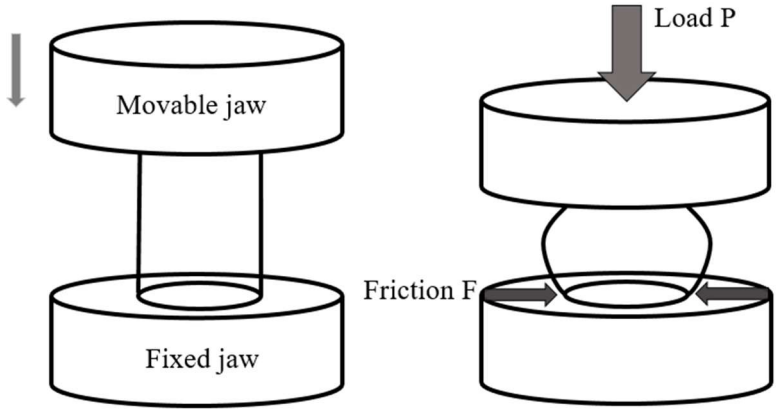

Fig. 2.1. A schematic of compression process showing effect of applied load and friction.

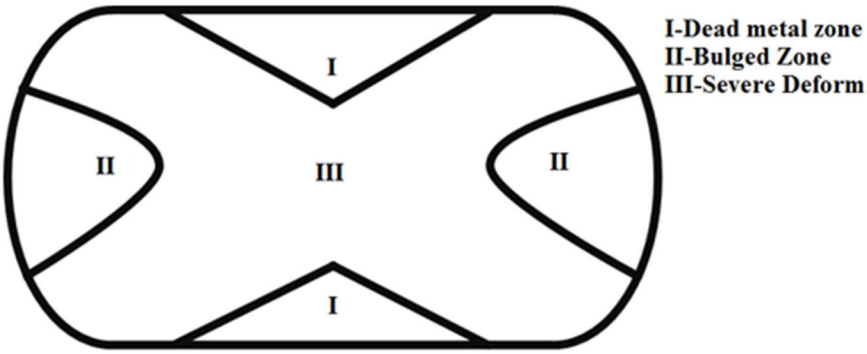

Fig. 2.2. Deformation zones of a hot compressed specimen.

Workability consists of two independent parts [3]:

1. Intrinsic workability: Hot working having substantial microstructural change is referred as intrinsic workability. It is sensitive to material chemistry, processing history and processing parameters.
2. State of stress workability: It exists in the deformation zone and depends on the applied state of stress and geometry of the deformation zone.

2.4 Materials modeling

The materials modeling is done with an aim to predict the constitutive behavior of material under certain given condition of processing. It is expected from a model to predict the microstructural evolution, flow resistance, process parameter limitations and its optimization.

2.4.1 Kinetic model

During hot deformation, steady state flow stress can be related to temperature and strain rate by an Arrhenius type equation [25] given by Eq. (2.1).

$$\dot{\varepsilon} = A\sigma^n \exp\left(-Q/RT\right) \qquad 2.1$$

Where $\dot{\varepsilon}$ is the strain rate, σ is flow stress, A is a coefficient, Q is the apparent activation energy, T the absolute temperature, n is the stress exponent and R is the universal gas constant.

2.4.2 Atomistic model

Raj [26] proposed numerous atomistic models to determine the limiting conditions of processing parameters like strain rate and temperature, which can be responsible for microstructural control during hot deformation. The four different processes were considered, namely

1. Void formation – Critical strain rate for void formation at hard particles is calculated.
2. Wedge cracking at grain boundary triple junction- Occurs at high temperature and low strain rates which promotes grain boundary sliding.
3. Adiabatic shear band formation – Modelled to find the regime of shear band formation.
4. DRX – It is modelled based on a kinetic approach to find out the onset of DRX.

To model the constitutive behavior of materials under hot deformation, this model was a revolutionary attempt for hot processing of materials.

2.4.3 Dynamic materials model (DMM)

Prasad et al. [6] proposed this model to describe the constitutive behavior of material, based on physical systems modeling, continuum mechanics of large plastic flow and irreversible thermodynamics. The DMM is described in detail in chapter 4.1.1.

2.5 Deformation induced ferrite transformation (DIFT)

The DIFT can take place during intercritical hot deformation of steels and results in extensive grain refinement. After austenitizing, the steel is undercooled to intercritical region and the metastable austenite is deformed. This $\gamma \rightarrow \alpha$ transformation is more advantageous than recrystallization of austenite at high undercooling. There are many other names used for DIFT like strain induced ferrite transformation (SIFT), dynamic ferrite transformation (DFT). It is called dynamic because of assumption that this $\gamma \rightarrow \alpha$ transformation occurs during the deformation. This is the most suitable technique to produce ultra-fine grained dual phase steel. The DIFT can be influenced by parameters like deformation temperature, strain, strain rate and prior austenite grain size.

Generally, in the $\gamma \rightarrow \alpha$ transformation, the ferrite nucleates at heterogeneous sites like edges, grain corners, surfaces etc. [27]. In deformed γ, this nucleation takes place inside the austenite grains and at the grain boundaries due to presence of shear bands, microbands, grain boundary misorientation etc. The stored energy in austenite due to work hardening increases the austenite to ferrite driving force.

2.6 Research gap and problem formulation

After reviewing the large number of available literatures, following research gaps were identified:

1. Studies on hot deformation of low alloy and plain carbon steel exist but there is lack of systematic treatment of low alloy steel especially at high strain rates.
2. There is lack of studies with a wide range of processing parameters and its discussion.
3. No studies exist which correlate of Zener-Hollomon parameter, processing map domains and flow curves.
4. The comparison of different material model processing map is also lacking.

5. Constitutive equation analysis exists but no attempt has been made to model the flow stress and materials constants to find its relation with true strain.

This work is mainly concerned with the modeling of flow behavior using constitutive relations, development of processing maps using different material model and correlation of its domains with the microstructures obtained after hot deformation of a low alloy medium carbon steel at different combination of temperature and strain rate at a fixed total true strain of 0.7.

The workability of the selected steel is required to be investigated by using the obtained data from uniaxial hot compression tests. Based on flow curves data, constitutive equations will be developed and modeling of flow stress will be done. The DMM and MDMM with different instability criteria will be used to plot the processing maps so as to optimize the processing parameters for hot working of this steel. The basic objectives of this research are as follows:

1. Hot compression testing of material in wide range of temperature (800-1050ºC) and strain rate (0.01-10 s^{-1}) at a fixed total true strain of 0.7.
2. To model the hot compression behavior and study the microstructural evolution after hot deformation.
3. To plot the processing maps using the Dynamic Materials Model (DMM), modified DMM and different instability criteria proposed by Prasad et al., Murty and Rao and Poletti et al.
4. To delineate the safe and the instability domains of processing parameters.
5. Determination of all material constants and activation energy at different strains and modeling of flow behavior to predict flow stress using constitutive equations.

On the basis of results of compression tests, an optimum processing parameter can be determined for efficient production with high productivity. The influence of processing parameters on different material constants and activation energy of hot deformation will be discussed. Also their effect on power dissipation efficiency and occurrence of defects and instability will be discussed.

CHAPTER 3

EXPERIMENTAL METHODOLOGY

In this section, the experimental methodology used in the present research is discussed. The experimental work involved a sequence of compression tests on Gleeble® 3800 Thermo-mechanical simulator followed by constitutive analysis, flow behavior modeling and characterization.

3.1 Material procurement

The steel cylindrical rod of 10mm diameter is obtained and its chemical composition is determined on Thermo-Jarrell Ash spark emission spectroscope. The obtained chemical composition is given in Table 3.1**.**

Table 3.1. Chemical composition of as-received steel (in wt. %).

Element	C	Si	Mn	P	S	Cr	Ni	Al	Cu	Fe
Wt. %	0.43	0.27	0.21	0.01	0.002	0.89	0.80	0.01	0.16	Bal.

3.2 Sample preparations

Specimens for the spark spectroscopy, dilatometry, hot compression tests and initial characterization (hardness and microstructure) were machined from the steel rod by parting and turning operations on a lathe machine. The cylindrical hot compression and dilatometry tests specimen dimensions were ϕ10mm x l5mm length and ϕ10mm x 70mm length, respectively. The aspect ratio was kept 1.5, in order to promote the homogeneous deformation without buckling [6]. The photograph of specimen before and after deformation is shown in Fig. 3.1.

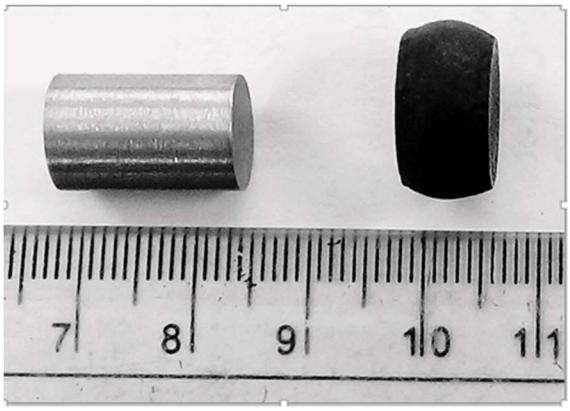

Fig. 3.1. Specimen before and after deformation hot compression test.

3.3 Experimental procedure

In this section, a brief description of the experimental methods and equipment used for different tests and analysis is given.

3.3.1 Initial characterization

The initial characterization of the as-received steel was done. The Vickers hardness measurements were carried out on the polished specimen on the FIE Vickers hardness tester (model VM 50) at a load of 10 kgf and dwell time of 15 seconds according to the ASTM E92-82 standard. The initial micrographs of specimen were taken on Leica DMI 5000M light optical microscope. The specimen was prepared following the standard procedure. The grinding of specimen was done followed by paper polishing on emery paper in sequence of P320, P800, P1200, P1500 and P2000 and then cloth polishing using alumina powder followed by etching with 2% nital. The abluent solution of saturated picric acid was used to reveal the prior austenite grain boundary.

3.3.2 Phase transformation characterization

To determine the phase transformation temperatures (critical temperatures) and to select the deformation temperatures, dilatometry tests were performed on Gleeble® 3800 with the help of CCT dilatometer with linear voltage differential transducer (LVDT). A CCT dilatometer model 39018 (Fig. 3.2) was used during the dilatometric tests. This model has fine adjustments to quartz measurement tip pressure, which helps to maintain its accuracy at high temperature. It has a linear range within ± 2.5 mm and a linearity of ± 0.25% full scale, and can hold specimens of 5 mm to 16 mm diameter. The measuring head of dilatometer was completely enclosed in the chamber under the vacuum, during the test.

Fig. 3.2. LVDT dilatometer with a range of ± 2.5 mm.

Fig. 3.3. Photograph of resistance spot welding machine.

A K-type thermocouple was spot welded at the midsection of the specimen for measuring and controlling the temperature during the test. Resistance spot welding machine (Fig. 3.3) was used for thermocouple welding. The specimen was austenitized to 1100ºC with a heating rate of 5ºCs^{-1}. The expansion in the specimen was recorded by LVDT quartz dilatometer and a plot of the change in length versus temperature shows the Ac_1 and Ac_3 temperatures.

3.3.3 Uniaxial hot compression test

Uniaxial isothermal hot compression test is the commonly used simple test to determine the hot workability of the material. Due to study of isothermal planes, it is considered that the test response will accurately replicate the material being tested, irrespective of its size. The hot compression tests were done in Gleeble® 3800 under vacuum (pressure of 1Pa) [14]. The temperature of the test specimen was monitored by a K-type thermocouple (200°C to 1260°C in which composition of chromel having 90% nickel and 10% chromium and alumel has 95% nickel, 2% manganese, 2% aluminium and 1% silicon) which was spot welded to the mid-section of the specimen. The adiabatic temperature rise in the specimen during the deformation was also measured by this thermocouple. To reduce the temperature gradient, friction and the barreling effect, nickel based lubricant with graphite foil were employed to the flat ends of the cylindrical specimen. It also helps in preventing the sticking of metal specimen with the tungsten carbide anvils during testing. The hot compression simulation scheme is shown in Fig. 3.4. Each specimen was heated to an austenitization temperature of 1100ºC at 5ºCs^{-1} and soaked for 2 min. Then they were cooled down with 1ºCs^{-1} cooling rate to each compression test temperature in the range of 800ºC-1050ºC, at increment of 50ºC. The specimens were deformed at different strain rate of 0.01, 0.1, 1, 10 s^{-1} up to a total true strain of 0.7. The justification of selecting austenitization temperature 1100ºC is because chromium carbide ($Cr_{23}C_6$ and Cr_7C_3) begins to dissolve at 900ºC and is completely in solution at 1100ºC. Finally, the compressed specimen was in-situ water quenched to avoid any meta-dynamic phenomena to occur and freeze the microstructure. For compression tests, true strain can be defined by following Eq. (3.1).

$$\varepsilon = \ln\left(\frac{h_o}{h_i}\right) \qquad 3.1$$

Where, h_i the instantaneous height of the specimen and h_o is the initial height of the specimen.

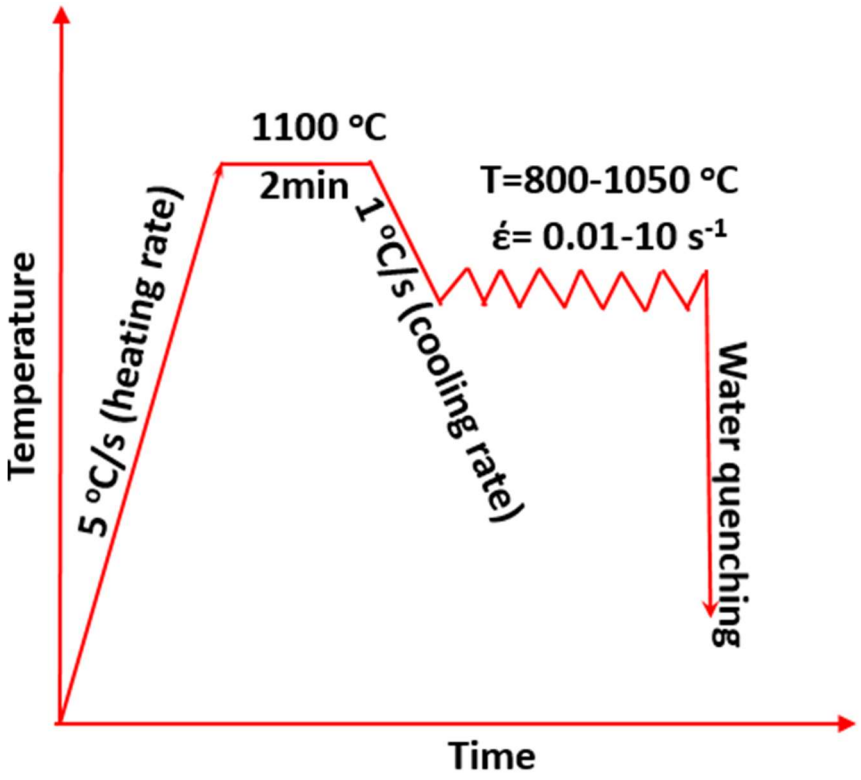

Fig. 3.4. Schematic of compression test showing parameters range.

3.4 Gleeble® 3800 simulator

Thermo-mechanical simulator is a testing machine which can physically simulate the high temperature tests with a high strain rate and helps in the study of high temperature behavior of metals and alloys. The external outlook of the TMS Gleeble® 3800 is shown in Fig. 3.5. It mainly consists of (a) the main control unit, (b) the testing unit, (c) the hydraulic power unit and (d) the vacuum pump unit.

It is a closed loop feedback system unit which controls and regulate the temperature using K-type thermocouple, spot welded at the longitudinal center of the specimen. The heating of the specimen is done by resistance heating using alternating current (AC). The heat is dissipated from the specimen by radiation and conduction from the flat ends, which are in contact with water-cooled jaws and the heat is maintained constant by heat input due to electrical resistance. The thermal gradient and friction during the test were reduced by using 5 mil thickness graphite between the ISO-T anvil and the specimen.

The actuator generates the force and displacement which are measured by a load cell and LVDT respectively, with an accuracy of ±0. 25% of the full scale. There is a calibration between applied force and output voltage to the load cell. The load cell provides an output

voltage of proportional magnitude to the applied force. The LVDT is attached at the base of the actuator and the movable core is positioned by the piston of the actuator. With the piston displacement from mid stroke position, the output voltage increases linearly. The stroke (a closed loop mechanical displacement control system) provides the capability to provide the constant strain rate deformation during the compression. The load cell of 50KN capacity and LVDT of gauge length 100mm was used in the present study.

The test specimen is placed between the fixed and movable jaw. The movable jaw is operated by a hydraulic-pneumatic system. The software tool like QuickSim makes easy for the operator to create any test as it provides the wave of arbitrary programming which work under different thermal and mechanical systems. The data acquisition rate is controlled by editing the program of the test so that 1000-5000 data would be recorded during each test.

Fig. 3.5. Hot deformation under Gleeble® 3800 thermomechanical simulator.

3.5 Microstructural characterization

The microstructural characterization of hot compressed specimen were done to study the change in grain size, shape and structure along with the occurrence of recrystallization. It was also helpful in study of the effects of processing parameters on the microstructure of the material. In this work, the microstructural evolution was studied using light optical microscopy (LOM) and scanning electron microscopy (SEM).

3.5.1 Optical microscopy

The light optical microscopy was employed for characterization of the studied material in as-received condition and after the hot deformation tests. The proper accuracy and interpretation of the obtained structure is mostly dependent on the sample preparations. A properly prepared specimen for optical microscopy must fulfill the following criteria:

1. The section must be free from stains, scratches and other imperfections.
2. All the non-metallic inclusions should be properly removed.
3. The section under study must be flat.

A Leica DMI 5000M microscope was used for LOM (Fig. 3.6). The phase fraction analysis and grain size measurement were done using Material plus 4.1 image analysis software. The following steps were followed for sample preparation of metallography:

1. Sectioning – The specimen after hot deformation were sectioned from the center along the compression axis using 'IsoMet 4000' high speed diamond saw (Fig. 3.7), to study the microstructure at the center of specimen where severe deformation occurred. The sectioned semicircular specimen was embedded in resin.
2. Grinding – It is required to prepare the specimen flat and remove the strained surface formed at the time of sectioning. P120, P320 and P600 grit SiC polishing papers were used in the given sequence by rotating the specimen 90º after polishing on each paper.
3. Paper Polishing – The strain free flat surface was paper polished using P800, P1200, P1500, and finally by using P2000 polishing papers. The specimen was washed by cold water and rotated by 90º after polishing on each paper.
4. Cloth polishing – The specimen after paper polishing was cloth polished on fine velvet cloth using alumina grade-I of size 0.014 μm. This process continued until the paper scratches disappeared.
5. Cleaning and Etching – To avoid the contamination between stages of polishing and cloth polishing, the specimen was washed using running cold water and then dried completely. The dried specimens were etched with 2% nital solution and saturated aqueous picric acid to reveal the microstructure. After etching, the specimen was quickly dried to prevent the staining and corrosion.

Fig. 3.6. Photograph of optical microscope (DMI 5000M).

Fig. 3.7. High speed diamond saw “IsoMet 4000”.

3.5.2 Scanning electron microscopy

EVO18 Zeiss scanning electron microscope (SEM) (Fig. 3.8) equipped with LaB6 filament was employed to study the microstructural evolution after hot deformation of specimens. The above mentioned steps were also followed during sample preparation for SEM.

Fig. 3.8. Photograph of EVO 18 Zeiss scanning electron microscope.

3.6 Hardness tests

Vickers hardness tests were performed to identify the phases present in the microstructure of specimen. The micro-hardness test were helpful in identification of the phases based on their hardness value. A load of 10kgf with dwell time of 15 s were employed in bulk hardness test on FIE VM 50 Vickers hardness tester. The indentation image is captured on computer screen and its measurement and analysis were done by using Vickers software to obtain the hardness values. The micro-hardness tests were employed a 10g of load on VMH104 Microhardness Tester. Ten readings were taken for each specimen and their average is reported with error analysis.

CHAPTER 4

BASIC THEORY AND ANALYSIS

4.1 Processing maps

Processing map is the graphical representation of the behavior of a material under hot working conditions on the axes of temperature and strain rate for a given fixed strain. The first deformation mechanism map was developed by Ashby [21] and then processing maps were developed based DMM by Prasad et al. [6]. The basic principle of the processing maps is interdisciplinary which includes the fundamental concepts of mechanics of large plastic flow, physical system modeling and deterministic chaos in dynamic system [15]. Different materials models for hot deformation are projected for prediction of material behavior in terms of microstructural evolution, parameters optimization with no any employment of trial and error method [3].

4.1.1 Dynamic materials model and its modification

DMM is considered as a bridge between the continuum mechanics of large plastic flow and the evolution of microstructure in the material. According to this material model, the specimen have following characteristics:

1. **Dynamic and nonlinear**: Flow stress, which is the system response under hot working condition varies non-linearly with dynamic variables.
2. **Irreversibility**: Large plastic flow in very small duration is irreversible and the microstructural change is also irreversible leads to the rate of entropy generation positive.
3. **Dissipative**: The total applied power should be dissipated and no significant storage of energy in the material/specimen.
4. **Sensitivity to initial conditions**: The response of deformation and its mechanism are largely dependent on the chemistry of the specimen, initial processing and applied processing parameters.
5. **Away from equilibrium**: Specimens under large deformation at elevated temperature cannot be in equilibrium because the applied strain value is not infinitesimally small increments.

In DMM, the physical analysis of power partitioning is done by strain rate sensitivity (m). The viscoplasticity in hot deformation originates when the power dissipation occurs by microstructural change of the specimen which does not directly leads to plastic deformation. It causes changes in potential energy due to the movement of atoms to other new positions (e.g. at grain boundary). The rate of change of potential energy is time and temperature dependent and is influenced by deformation temperature and strain rate. At a given deformation temperature, the dissipation of total power ($P = \sigma \dot{\varepsilon}$) is directly proportional to the rate of entropy generation, which is positive for an irreversible thermodynamic process given by Eq. (4.1). The total power or entropy consists of two complementary functions, G 'dissipater power content', the power dissipated due to plastic deformation i.e. the movement of dislocations and J 'dissipater power co-content, the power dissipated through microstructural changes. Several metallurgical processes like DRY, DRX, internal cracks, dissolution of particles and phases, nucleation and growth of new grains or phases, deformation induced phase transformation etc. leads to change in the dissipated power co-content (J). The power partition areas G and J are shown in Fig. 4.1 by a flow stress-strain rate curve for a fixed given strain and deformation temperature and analytically expressed by Eq. (4.2).

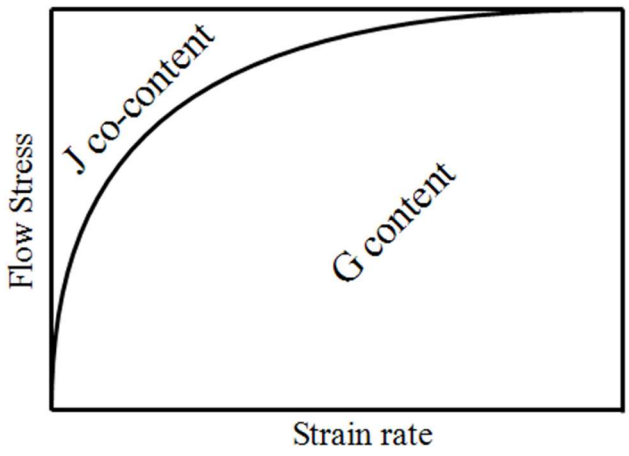

Fig. 4.1. Power partitioning as G-content and J co-content in material response [3].

$$P = \bar{\sigma}\bar{\dot{\varepsilon}} = T\frac{dS}{dt} \geq 0 \qquad 4.1$$

Where $\bar{\sigma}$ and $\bar{\dot{\varepsilon}}$ denotes the effective stress and strain rate

$$P = G + J = \int_0^{\dot{\varepsilon}} \sigma d\dot{\varepsilon} + \int_0^{\sigma} \dot{\varepsilon} d\sigma = \sigma\dot{\varepsilon} \qquad 4.2$$

According to the dynamic constitutive equation, ($\sigma = k.\dot{\varepsilon}^{m} l_{T,\varepsilon,M}$), for a given applied strain, temperature and initial microstructure, the energy partitioning between G and J is determined by the strain rate sensitivity parameter (m) [13] as given in Eq. (4.3)

$$m = \left(\frac{\partial J}{\partial G}\right)_{T,\varepsilon} = \frac{\sigma d\dot{\varepsilon}}{\dot{\varepsilon} d\sigma} = \left[\frac{\partial \ln \sigma}{\partial \ln \dot{\varepsilon}}\right]_{T,\varepsilon} \quad 4.3$$

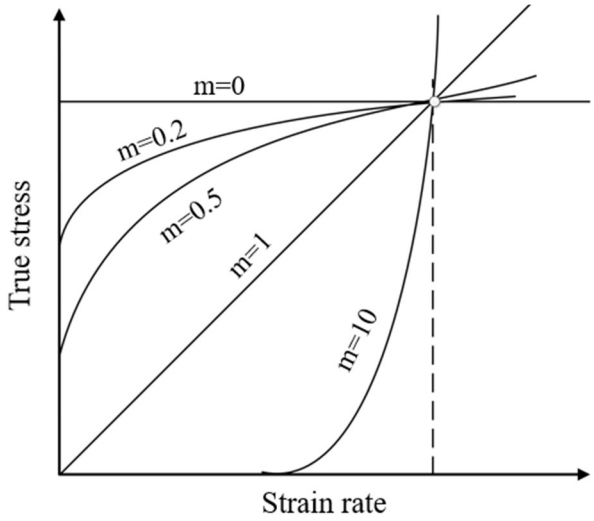

Fig. 4.2. Behavior of viscoplastic solid with the 'm' on the either side of unity [3].

The flow behavior under deformation having different value of 'm' for viscoplastic solids are illustrated by Ziegler [28] as shown in Fig. 4.2. The significance of values of *m* for a different flow behavior.

1. m=0; the power dissipation by metallurgical process is zero and the total power dissipation takes place as temperature rise caused due to movement of dislocation.
2. m=1; the material acts as viscous fluid like a superplastic flow of material.
3. 0<m<1; stable flow during plastic work.
4. m>1; the solids are called 'locking solids' and power law fails. The stress - strain curvature reversed and at a critical strain rate, the flow curve upsurges steeply and become independent of strain and strain rate.

Based on this power partition, the DMM described two parameters namely, the power dissipation efficiency η and the instability parameter ξ. For any given deformation temperature, the power co-content *J* is given by Eq. (4.4) [3]. The effect of J on plastic flow of materials can be described by the power dissipation efficiency defined as the ratio of J and the J_{max} possible when m=1, a linear dissipater (Eq. 4.5). This parameter η describes the power dissipation ability of material under applied power input.

$$J = \int_0^{\sigma} \dot{\varepsilon} d\sigma = \frac{\sigma.\dot{\varepsilon}.m}{m+1} \quad 4.4$$

$$\eta_{\Pr asad} = \frac{J}{J_{\max}} = \frac{2m}{(m+1)} \quad 4.5$$

Since the principle of DMM is based on power law, it breaks down at high value of stress. Murty and Rao [7] modified the calculation of the power dissipation efficiency to avoid the use of strain rate sensitivity. This modified DMM model gives useful results for multiphase materials. The efficiency $\eta_{\text{Murty and Rao}}$ is given by Eq. (4.6) and the G can be calculated as given by Eq. (4.7).

$$\eta_{Murty\,\&\,Rao} = \frac{2J}{P} = \frac{2(P-G)}{P} = \frac{2\left(1 - \int_0^{\dot{\varepsilon}} \sigma d\dot{\varepsilon}\right)}{\sigma\dot{\varepsilon}} \quad 4.6$$

$$G = \int_0^{\dot{\varepsilon}} \sigma d\dot{\varepsilon} = \int_0^{\dot{\varepsilon}_{\min}} \sigma d\dot{\varepsilon} + \int_{\dot{\varepsilon}_{\min}}^{\dot{\varepsilon}} \sigma d\dot{\varepsilon} = \left[\frac{\sigma\dot{\varepsilon}}{m+1}\right]_{\dot{\varepsilon}=\dot{\varepsilon}_{\min}} + \int_{\dot{\varepsilon}_{\min}}^{\dot{\varepsilon}} \sigma d\dot{\varepsilon} \quad 4.7$$

The selection of a proper instability criterion is very important so as to know the extent of plastic deformation of the material before the formation of defects. Ziegler's instability criteria based on continuum principle [29] suggested that flow instability occurs when,

$$\frac{\partial D}{\partial \dot{\varepsilon}} < \frac{D}{\dot{\varepsilon}} \quad 4.8$$

where, D is the power dissipation function.

Based on Eq. (4.8), the instability criteria calculation is dependent on the formulation of dissipation function. Prasad [15] used D=J, which considers only the metallurgical power dissipation and proposed an instability criteria given in Eq. (4.9). The instability criteria (k) suggested by Murty and Rao is given by Eq. (4.10). Poletti et al. [8] also proposed an instability criteria (k_j), to avoid the dependence on strain rate sensitivity given by Eq. (4.11).

$$\xi_{\Pr\,asad} = \left(\frac{\partial \ln\left(m/m+1\right)}{\partial \ln(\dot{\varepsilon})}\right) + m < 0 \quad 4.9$$

$$\kappa = \frac{2m}{\eta} - 1 < 0 \quad 4.10$$

$$\kappa_j = \left(\frac{\partial \ln J}{\partial \ln \dot{\varepsilon}} - 1\right) < 0 \quad 4.11$$

The curve ξ=0, delineates the stable plastic flow and instability and its negative value provides the instability domains. Similarly the negative values of k and k_j shows the instability region in the processing maps. The variation of η (power dissipation efficiency) with temperature and strain rate represents the constitutive flow behavior and establishes a 3-D contour power dissipation map. The instability criteria when plotted and superimposed on the obtained power dissipation map, it delineates the instability domains and provides the processing maps.

4.2 Constitutive equation

The processing parameters like strain rate, temperature and flow stress are interdependent and follow the given form of kinetic rate equation (Eq. 4.12)

$$\sigma = K\varepsilon^n \dot{\varepsilon}^m + Y \qquad 4.12$$

where K and Y are coefficients and n is the strain hardening exponent.

The significance of m and n varies with the temperature. For low temperature, strain hardening exponent becomes significant and for elevated temperature, strain rate sensitivity becomes significant. But the above Eq. (4.12) does not show any effect of temperature. Therefore, Zener-Hollomon Parameter, a temperature compensated strain rate, correlates between temperature and constitutive equations. At low stresses, the hot deformation behavior is governed by power creep law (Eq. 4.13) and at high value of stresses, the exponential law is used (Eq. 4.14). The hyperbolic sine law is applicable to all values of flow stress and is also referred as universal constitutive equations (Eq. 4.15). All these three equations correlate the stress, temperature and strain rate in hot working of materials.

$$Z = \dot{\varepsilon} \exp\left(\frac{Q}{RT}\right) = C\,\sigma^{n'} \qquad \alpha\sigma < 0.8 \qquad 4.13$$

$$= B\exp(\beta\sigma) \qquad \alpha\sigma > 1.2 \qquad 4.14$$

$$= A[\sinh(\alpha\sigma)]^n \qquad \text{For all } \sigma \qquad 4.15$$

Where, R is the universal gas constant (8.314 J/mole/K), Q is the apparent activation energy (kJ mole^{-1}), T is the absolute temperature in K; and A, B, C, n, n', β, and α=β/n' are material constants**.**

CHAPTER 5
RESULTS AND DISCUSSION

This chapter focuses on the study of hot deformation behavior of low alloy medium carbon steel at different temperature and strain rate ranges and its prediction by using the constitutive equations analysis. The adiabatic heating correction of the experimental true stress-strain curve is done followed by modeling of flow stress for its prediction. The processing maps based on different material models are plotted and their domains are discussed and correlated with the microstructure obtained. Also, the safe and instability domains are identified which can help in avoiding defects.

5.1 Initial characterization

The initial characterization consists of tensile test, hardness, as-received microstructure and the critical temperatures for phase transformations. The hardness of as-received steel is found 272VHN at a load of 10kgf. The critical temperatures were determined by dilatometry test (CCT) on TMS using Quartz dilatometer and also by other methods. The critical temperatures obtained on TMS, L75 dilatometer, empirical method and by thermo-calc are tabulated in Table 5.1. The result of CCT test shows that as temperature increases, the dilation in the specimen increases up to 752ºC and then decreases upto 823ºC due to formation of austenite (contraction occurs), further it increased after complete formation of austenite Fig. 5.1. The variations in slope of curve represents the onset of phase transformation. The Ac_3 and Ac_1 temperatures for this steel are 823ºC and 752ºC respectively.

Table 5.1. Critical temperatures of steel determined by different methods.

S. no.	Methods	Ac_1 (ºC)	Ac_3 (ºC)
1.	Dilatometry (TMS)	752	823
2.	L75 Horizontal dilatometer	758	804
3.	Empirical method	726	777
4.	Thermo-calc software	716	761

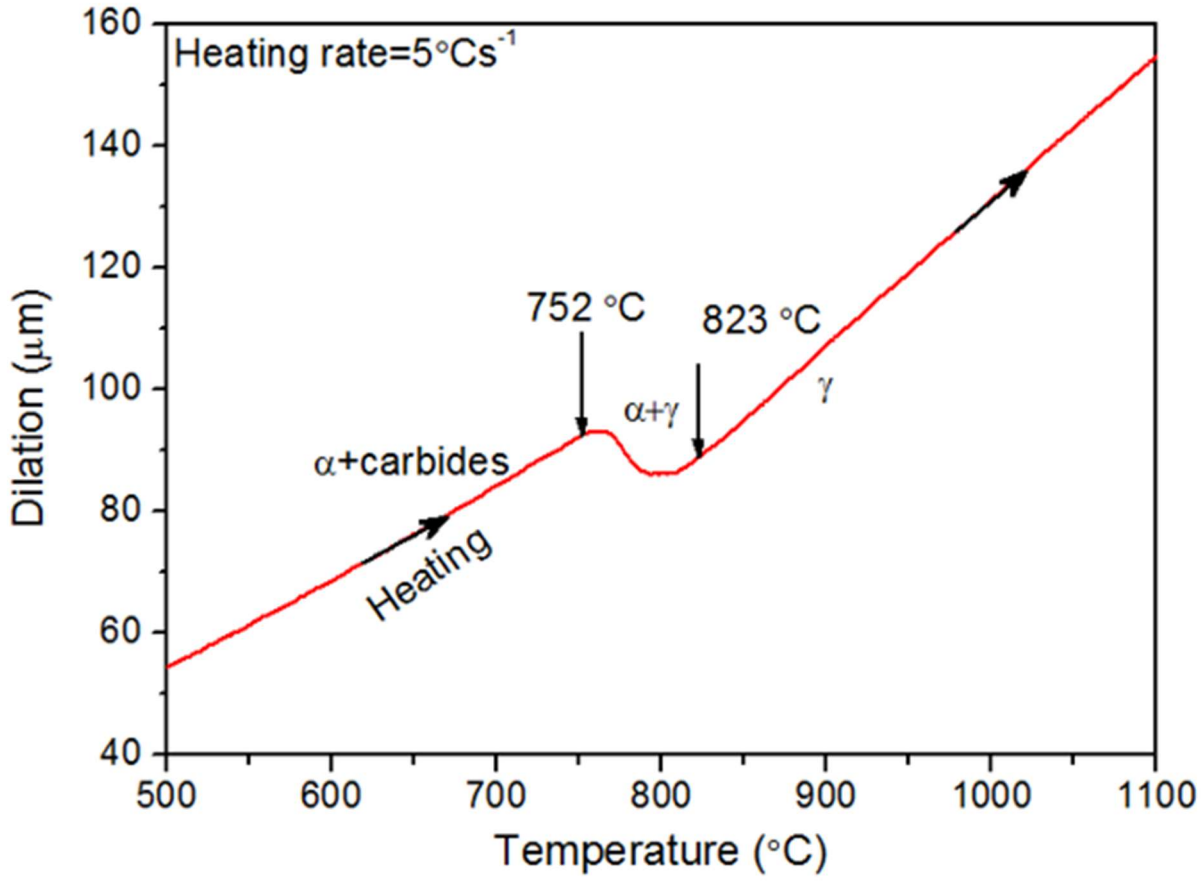

Fig. 5.1. Result of the dilatometry test (TMS) showing the critical temperatures Ac_1 (752ºC) and Ac_3 (823ºC).

The tensile test specimen of as-received steel after tensile test is shown in

Fig. 5.2 which results ultimate tensile strength (UTS) of 838 MPa and elongation of 13%.

Fig. 5.2. Image of specimen after tensile test.

The microstructure of as-received steel specimen is shown in Fig. 5.3. The microstructure consists of bright phase which is ferrite and the dark phase having lamellar structure is pearlite (shown by arrows).

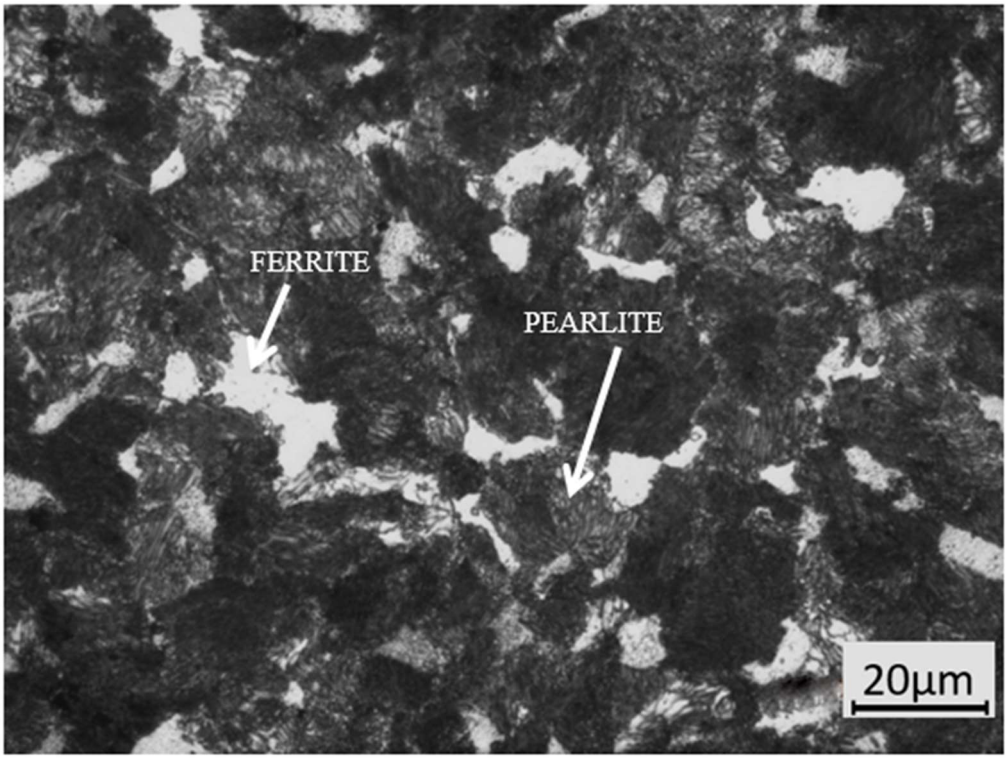

Fig. 5.3. Optical micrograph of as-received steel specimen.

5.2 True stress-true strain curves

The temperature range of tests were 800ºC-1050ºC with an increment of 50ºC and strain rate range of 0.01-10 s^{-1}. During plastic deformation, materials produces heat which is either dissipated to the surrounding or increases the temperature when rate of heat generation is more than rate of heat dissipation. The maximum increment in temperature due to adiabatic heating are tabulated in Table 5.2 as a function of strain rate and temperature. The largest increment (dT) values are observed at low temperatures and high strain rates.

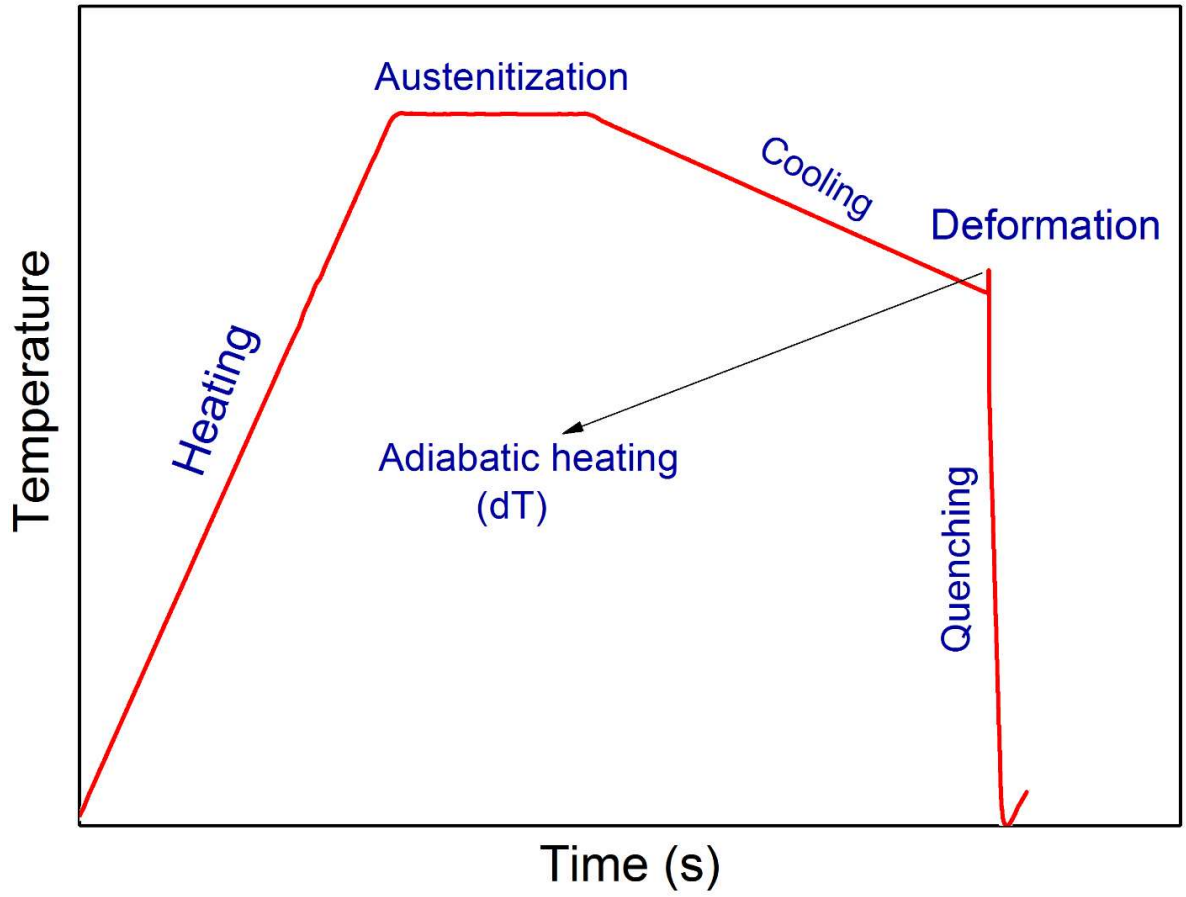

Fig. 5.4. Schematic showing adiabatic temperature rise during deformation.

Table 5.2. Maximum temperature increment (dT) during hot compression of LAMCS.

Deformation Temperature(°C)	**dT (°C) at strain rates (s^{-1})**			
	0.01	**0.1**	**1**	**10**
800	3	6	25	32
850	5	10	28	27
900	5	12	15	26
950	3	9	12	23
1000	6	6	13	18
1050	3	5	9	19

The adiabatic heating corrected and experimentally obtained true stress-true strain flow curves are plotted as shown in Fig. 5.5 to study the flow behavior and effect of adiabatic heating during deformation. The adiabatic heating correction were done using linear interpolation method between ln(σ) and 1/T (T is in K) at a constant strain rate and strain [30]. It can be observed

that the flow curves are dependent on strain rate and temperature. At a fixed strain rate, with increase in deformation temperature, the flow stress decreases progressively (Fig. 5.6a). This happens because at high temperature mobility of dislocation increases. Similarly, for a fixed temperature, as the value of strain rate increases the flow stress also increases as shown in Fig. 5.6b. The peaks in the flow curves shifted to higher strain as the hot compression temperature decreased or the strain rate increased [14]. The deformation process may be dislocation generation (strain hardening) and dislocation annihilation (strain softening) and if these two balances each other a steady state plateau is observed in flow curves. Dynamic recovery (DRV) and dynamic recrystallization (DRX) are the restoration mechanism during hot working which affect the flow behavior. The peak in flow curve shows the beginning of dynamic recrystallization and the flow curves without a stress peak represent dynamic recovery as softening mechanism. When Zener-Hollomon parameter (Z) is high, DRV occurs whereas when its value is low, DRX occurs. Dynamic recrystallization and dynamic recovery during hot deformation yields high heat dissipation efficiency 'η' and hence shows good hot workability.

The true stress-strain curves (850ºC–1050ºC, 0.01 s^{-1}–0.1 s^{-1}; 950 ºC–1050ºC, 1 s^{-1} and 1050ºC, 10 s^{-1}) exhibits a peak due to work hardening followed by softening to a steady state. The flow curves (800ºC and 0.01 s^{-1}–10 s^{-1}) do not have any peak and the work hardening is balanced by dynamic recovery softening mechanism to achieve a steady state. At 1050ºC and 0.01 s^{-1} the flow curve have multiple peaks and hence shows multiple peak DRX [8, 29].

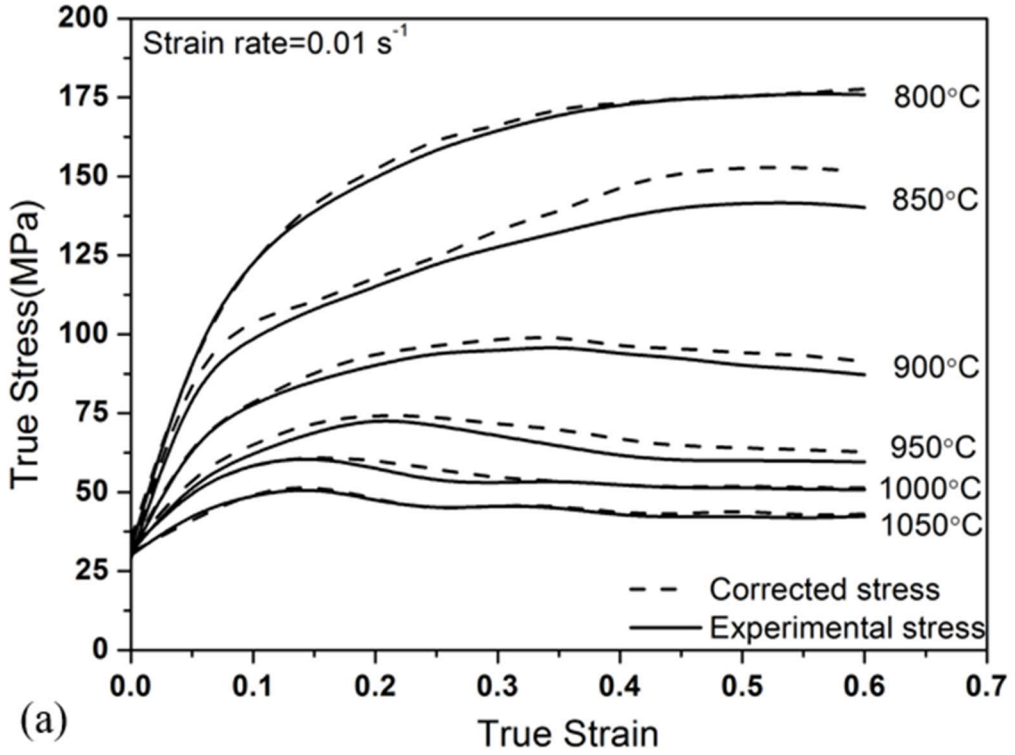
Strain rate=0.01 s-1
800°C
850°C
900°C
950°C
1000°C
1050°C
Corrected stress
Experimental stress
True Stress(MPa)
True Strain
0
25
50
75
100
125
150
175
200
0.0
0.1
0.2
0.3
0.4
0.5
0.6
0.7

(a)

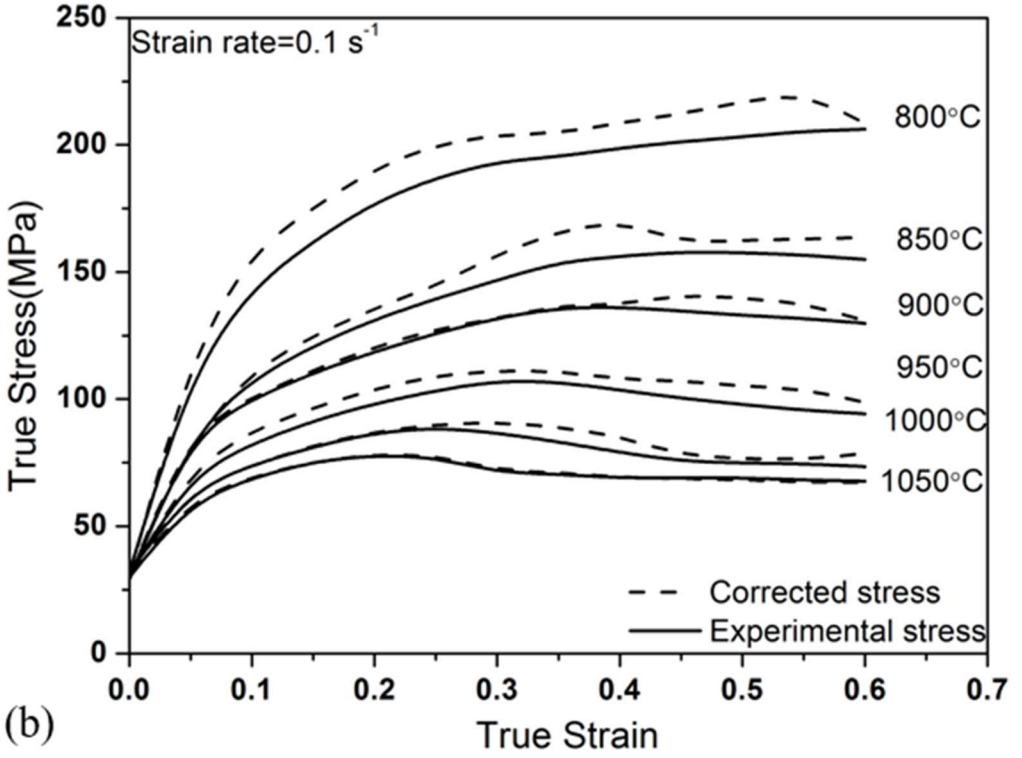
Strain rate=0.1 s-1
800°C
850°C
900°C
950°C
1000°C
1050°C
Corrected stress
Experimental stress
True Stress(MPa)
True Strain
0
50
100
150
200
250
0.0
0.1
0.2
0.3
0.4
0.5
0.6
0.7

(b)

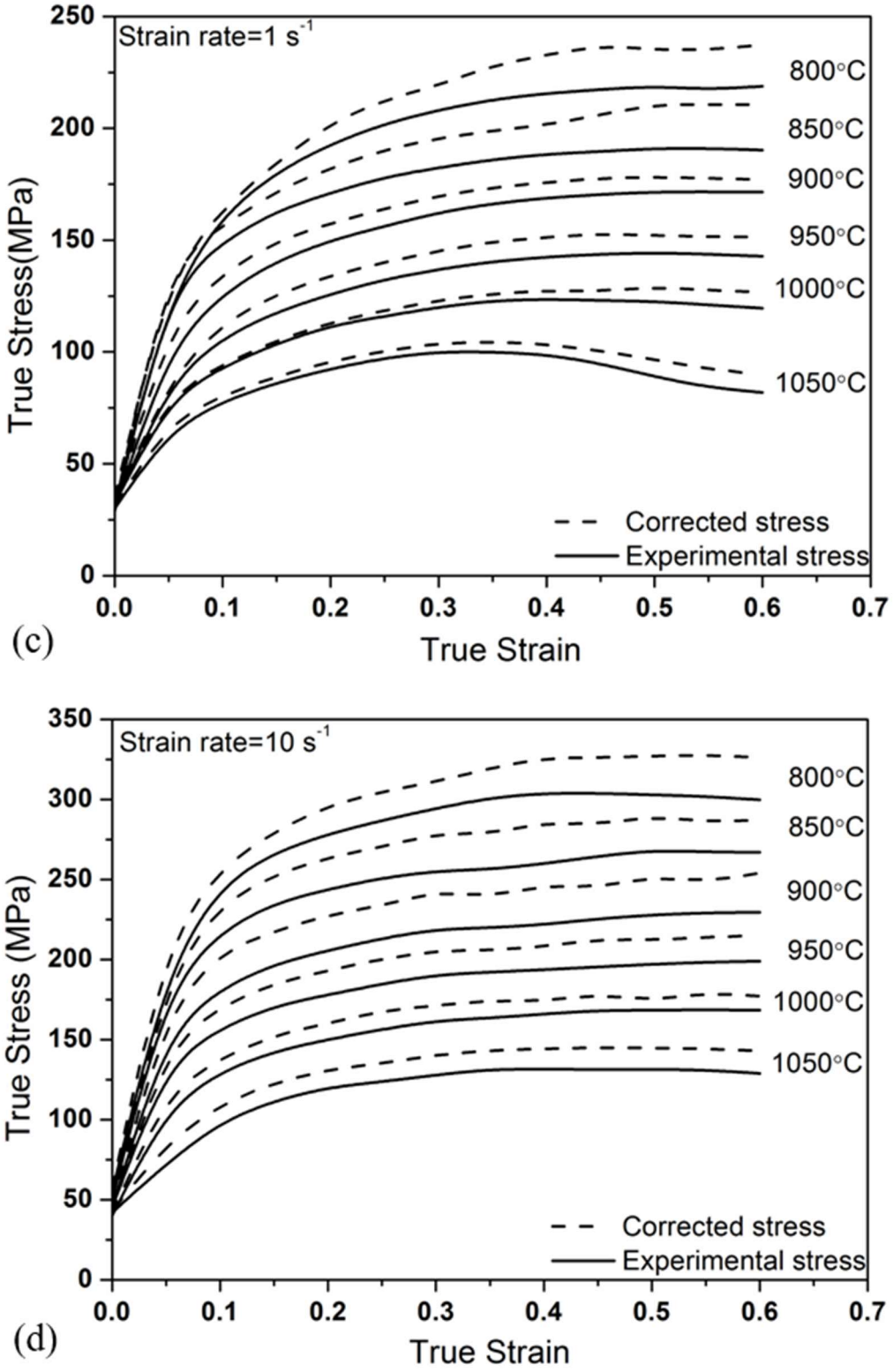

Fig. 5.5. True Stress-Strain curves of specimens deformed at temperature range of 800-1050ºC at (a) 0.01 s^{-1}, (b) 0.1 s^{-1}, (c) 1 s^{-1} and (d) 10 s^{-1}.

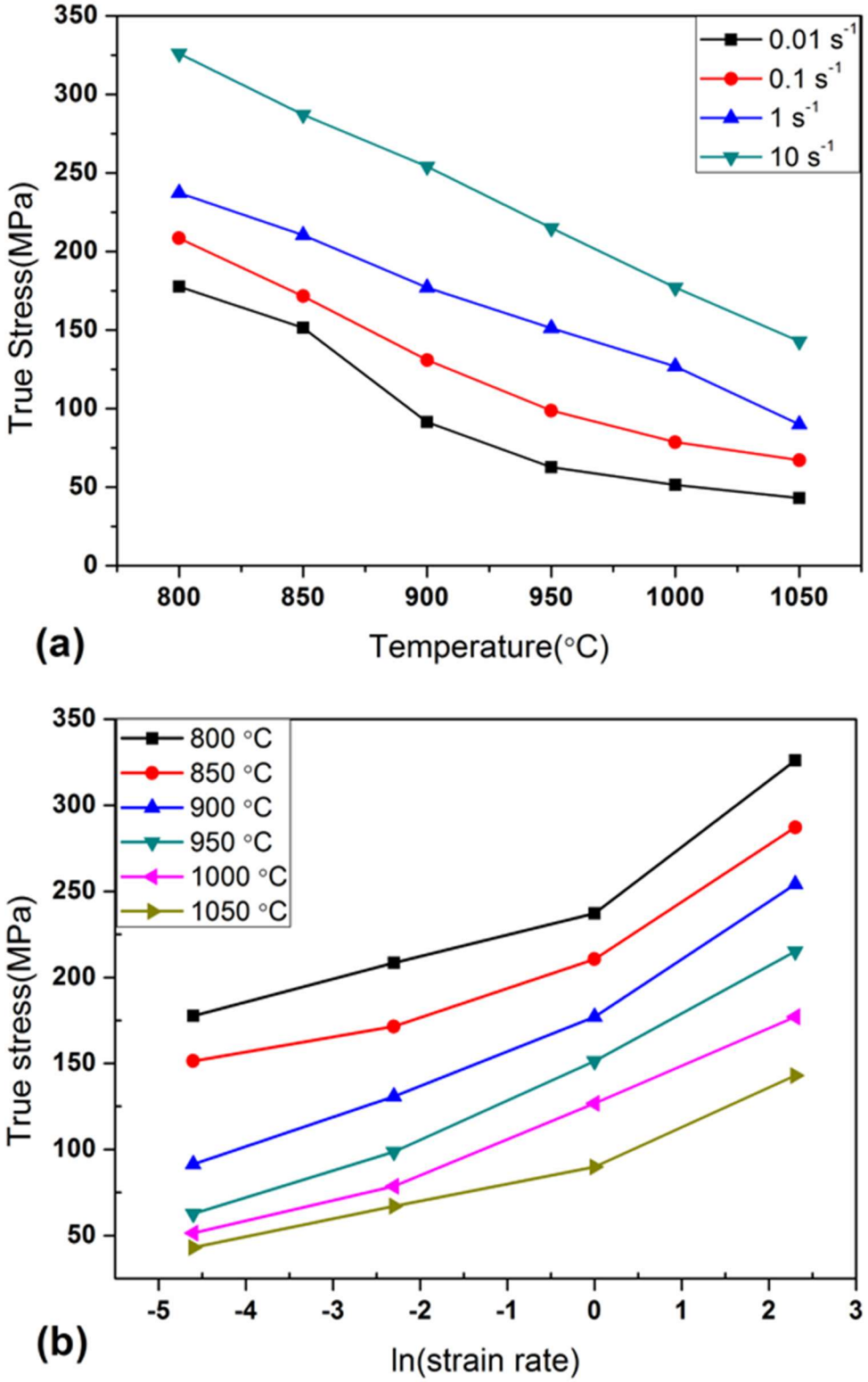

Fig. 5.6. Relationship between flow stress and (a) deformation temperature and (b) the logarithmic of applied strain rate.

5.3 Constitutive equation analysis

The deformation mechanisms can be studied using constitutive equation analysis. To find out all the material constants, taking logarithm on both sides of Eqs. (4.13), (4.14) and (4.15) we get

$$\ln\dot{\varepsilon}+\left(\frac{Q}{R}\right)\left(\frac{1}{T}\right)=\ln C+n'\ln\sigma \tag{5.1}$$

$$\ln\dot{\varepsilon}+\left(\frac{Q}{R}\right)\left(\frac{1}{T}\right)=\ln B+\beta\sigma \tag{5.2}$$

$$\ln\dot{\varepsilon}+\left(\frac{Q}{R}\right)\left(\frac{1}{T}\right)=\ln A+n\ln\left[\sinh(\alpha\sigma)\right] \tag{5.3}$$

For isothermal hot compression process, the partial differentiation of Eqs. (5.1), (5.2) and (5.3) provide the following equations respectively.

$$n'=\left[\frac{\partial\ln\dot{\varepsilon}}{\partial\ln\sigma}\right]_T \tag{5.4}$$

$$\beta=\left[\frac{\partial\ln\dot{\varepsilon}}{\partial\sigma}\right]_T \tag{5.5}$$

$$n=\left[\frac{\partial\ln\dot{\varepsilon}}{\partial\ln\{\sinh(\alpha\sigma)\}}\right]_T \tag{5.6}$$

These expressions represent that the slope of $\ln\dot{\varepsilon}$ versus $\ln\sigma$ and the slope of $\ln\dot{\varepsilon}$ versus σ can be used to obtain the value of n' and β respectively. The flow stress data used for analysis was obtained from flow curves at 0.6 true strain. The mean of the slopes were taken and the value of n' and β was found to be 7.5774 and 0.04999 MPa^{-1} respectively as shown in Fig. 5.7 (a) & (b). This provides $\alpha=\beta/n'=0.006598$ MPa^{-1}. From Eq. (5.6), the slope of $\ln\dot{\varepsilon}$ vs ln (sinh (ασ)) provides the value of n as shown in Fig. 5.7 (c). The average value of slopes provides the average value of n as 5.4. This value of stress exponent (n), indicates that the deformation mechanism is dislocation glide controlled by dislocation climb [32]. Among Arrhenius type equations, the sinh type law provides superior estimation between Zener-Hollomon parameter and flow stress for all range of stress [33]. The hot deformation activation energy for a constant strain rate based on universal constitutive equation, can be obtained by partially differentiating Eq. (5.3) which yields following equation:

$$Q = Rn\left[\frac{\partial \ln(\sinh(\alpha\sigma))}{\partial\left(\frac{1}{T}\right)}\right]_{\dot{\varepsilon}} \qquad 5.7$$

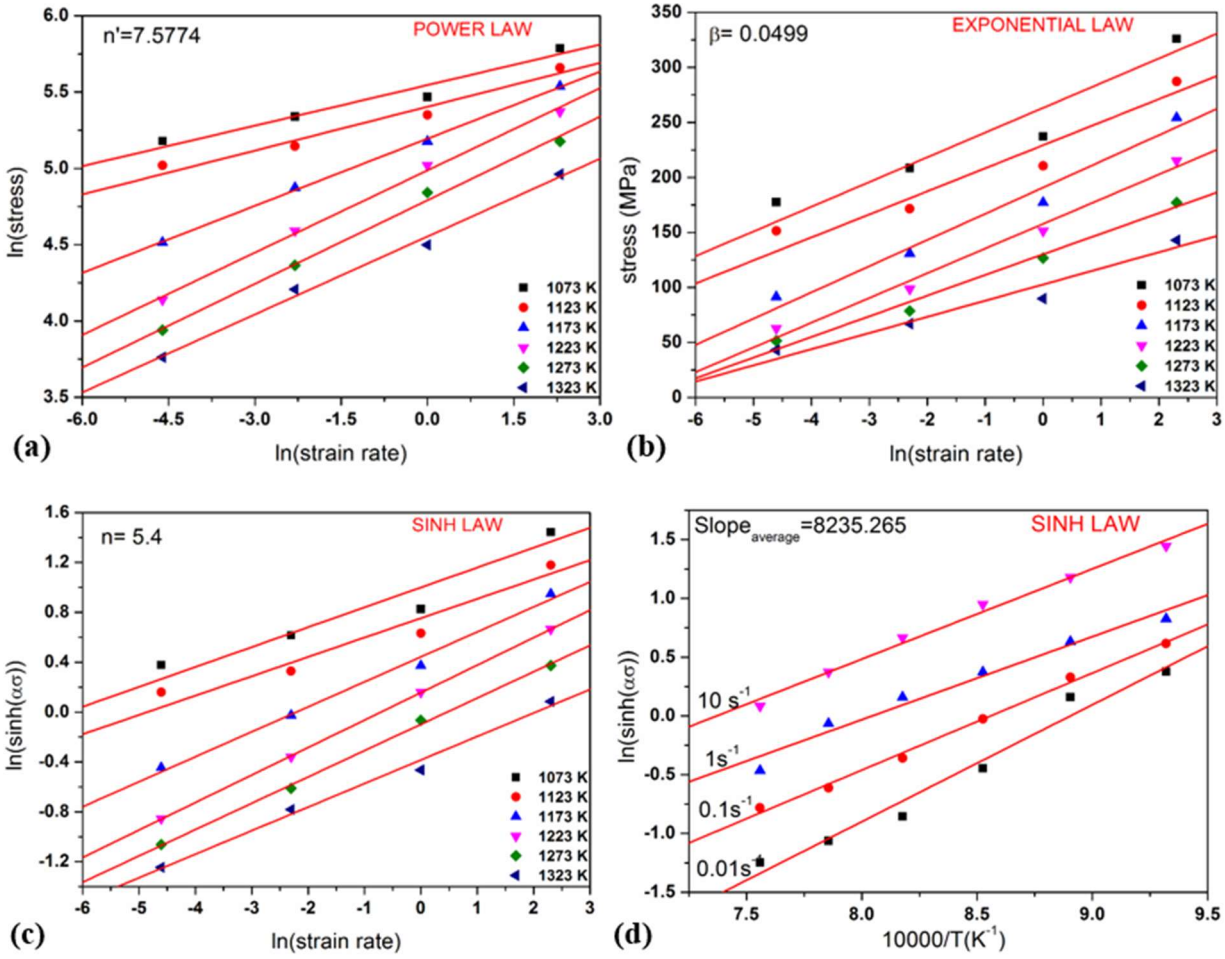

Fig. 5.7. Plots between ln(strain rate) and (a) ln(stress); (b) stress; (c) ln(sinh(ασ)) to find out the material constants n', β and n respectively and (d) ln(sinh(ασ)) versus reciprocal of absolute temperature (T) to obtain slope for activation energy calculation.

The slope of ln (sinh (ασ)) versus reciprocal of absolute temperature (T) based on Eq. (5.7) is shown in Fig. 5.7 (d). The average value of slope was found to be 8235.265 and the apparent activation energy corresponding to Eq. (5.7) was found to be 368.1 kJmol^{-1}. Similar values of apparent activation energy was reported by Zhang et al. [34] for medium carbon micro-alloyed steel. This value of apparent activation energy is larger than the self-diffusion activation energy of austenitic steel (311.1 kJmol^{-1}) due to the influence of alloying elements having low stacking fault energy [35].

By taking logarithm on both sides of Eq. (4.15) and putting the values of the strain rate, temperatures and flow stress for true strain of 0.6, the linear relationship between ln [sinh ($\alpha\sigma$)] and ln (Z) can be obtained as shown in Fig. 5.8, whose intercept yields the value of material constant A as 2.619 x 10^{15} s^{-1}. The correlation coefficient (R^2=0.987) was found to be maximum in case of universal constitutive equation which shows a better agreement with experimental data. Finally, substituting all the values of material constants and activation energy in Eq. (4.15), we get the constitutive relation for this steel at 0.6 true strain, which is expressed by Eq. (5.8).

$$Z = \dot{\varepsilon}\exp\left(\frac{368.1x10^3}{RT}\right) = 2.619x10^{15}\left[\sinh(0.006598\sigma)\right]^{5.4} \qquad 5.8$$

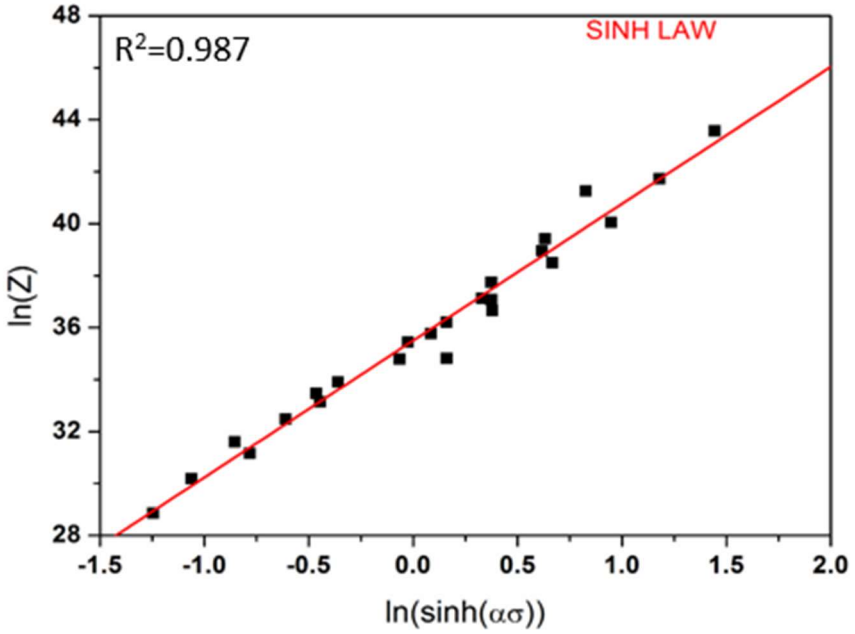

Fig. 5.8. Relationship between ln(Z) vs ln(sinh($\alpha\sigma$)) at true strain of 0.6.

5.3.1 Prediction of flow stress

It is assumed that strain has negligible effect on high temperature flow behavior and hence not considered in Arrhenius type equations [36]. The material constants (β, α, n, Q and ln(A)) of the constitutive relations were calculated for deformation strains ranging 0.05-0.6 at an interval of 0.05 by the same route as described above for 0.6 strain. Assuming the material constants as polynomial function of strains (Eq. 5.9), and polynomial fitted by varying degree from 3 to 6. A five degree polynomial having highest correlation coefficients has best fit to calculate data. From Fig. 5.9, it can be observed that β, α, n, Q and ln(A) have significant variation with strain. Coefficients β, α, and n are decreasing exponentially and activation energy and ln(A) are

increasing with increasing true strain. The activation energy varies from 311 kJmol^{-1} at true strain 0.1 to 368 kJmol^{-1} at true strain of 0.6.

The numerical values of coefficients by polynomial fitting of β, α, n, Q, and $\ln(A)$ of LAMCS are represented in Table 5.3. Based on sinh type law, from Eq. (5.8) the flow stress (σ) as a function of Zener-Hollomon parameter (Z), can be expressed as Eq. (5.10).

$$\begin{aligned}
\beta &= B_0 + B_1\varepsilon + B_2\varepsilon^2 + B_3\varepsilon^3 + B_4\varepsilon^4 + B_5\varepsilon^5 \\
\alpha &= C_0 + C_1\varepsilon + C_2\varepsilon^2 + C_3\varepsilon^3 + C_4\varepsilon^4 + C_5\varepsilon^5 \\
n &= D_0 + D_1\varepsilon + D_2\varepsilon^2 + D_3\varepsilon^3 + D_4\varepsilon^4 + D_5\varepsilon^5 \\
Q &= E_0 + E_1\varepsilon + E_2\varepsilon^2 + E_3\varepsilon^3 + E_4\varepsilon^4 + E_5\varepsilon^5 \\
\ln(A) &= F_0 + F_1\varepsilon + F_2\varepsilon^2 + F_3\varepsilon^3 + F_4\varepsilon^4 + F_5\varepsilon^5
\end{aligned} \tag{5.9}$$

$$\sigma = \frac{1}{\alpha}\ln\left\{\left(\frac{Z}{A}\right)^{1/n} + \left[\left(\frac{Z}{A}\right)^{2/n} + 1\right]^{1/2}\right\} \tag{5.10}$$

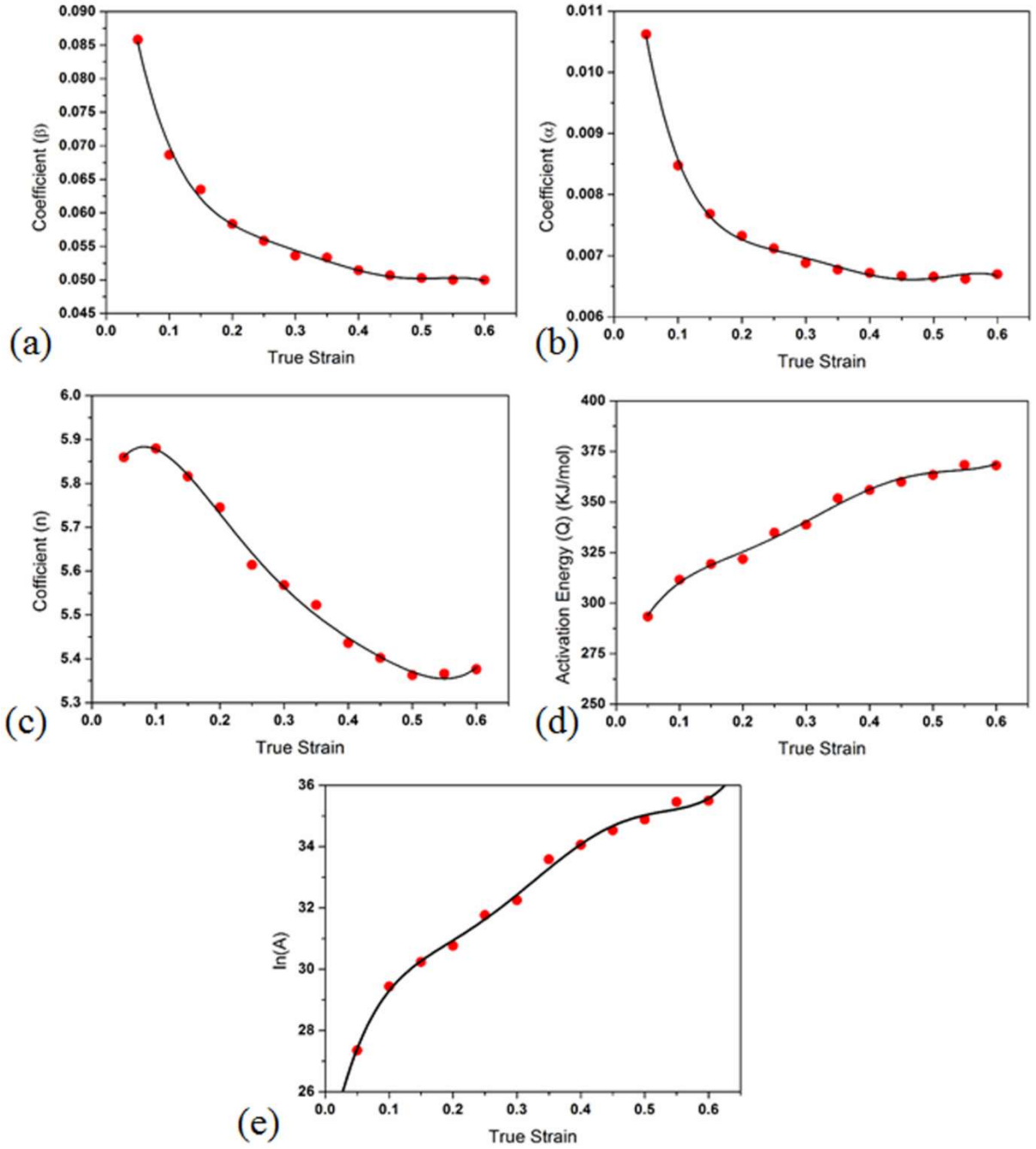

Fig. 5.9. Relationships between true strain and (a) β, (b) α, (c) n, (d) Q, and (e) ln(A) using five degree polynomial fit for a LAMCS.

Table 5.3. Results of five degree polynomial fit coefficients of β, α, n, Q and ln (*A*).

β		**α**		**n**		**Q**		**ln(A)**	
B_0	0.1138	C_0	0.0145	D_0	5.6957	E_0	261.996	F_0	23.6351
B_1	-0.7422	C_1	-0.1044	D_1	5.3822	E_1	873.4672	F_1	103.0235
B_2	4.0079	C_2	0.5977	D_2	-48.9446	E_2	-5583.8055	F_2	-652.618
B_3	-11.1358	C_3	-1.7049	D_3	154.1774	E_3	19485.0660	F_3	2207.86
B_4	15.1132	C_4	2.3478	D_4	-223.242	E_4	-30979.4865	F_4	-3424.29
B_5	-7.9061	C_5	-1.2399	D_5	124.8071	E_5	17993.8009	F_5	1954.242

5.3.2 Validation of developed constitutive equations

To verify the determined constitutive equations for LAMCS under hot compression at high temperatures, the experimental and predicted flow stress are compared. Using the above obtained values of material constants and activation energy at different strains between 0.05-0.6 at interval of 0.05 in Eq. (5.10), the predicted value of flow stress are calculated for entire given range of strain rates and temperatures. The experimental and predicted values of flow stress are plotted at six temperatures under strain rates of 0.01 s^{-1}-10 s^{-1} and compared as shown in Fig. 5.10. It can be observed from the comparison that the established constitutive relation has very good predictability of the flow stress. Hence, the developed constitutive equation for LAMCS is very helpful during inspection of the problems and identification of mechanisms of deformation at the time of hot working process.

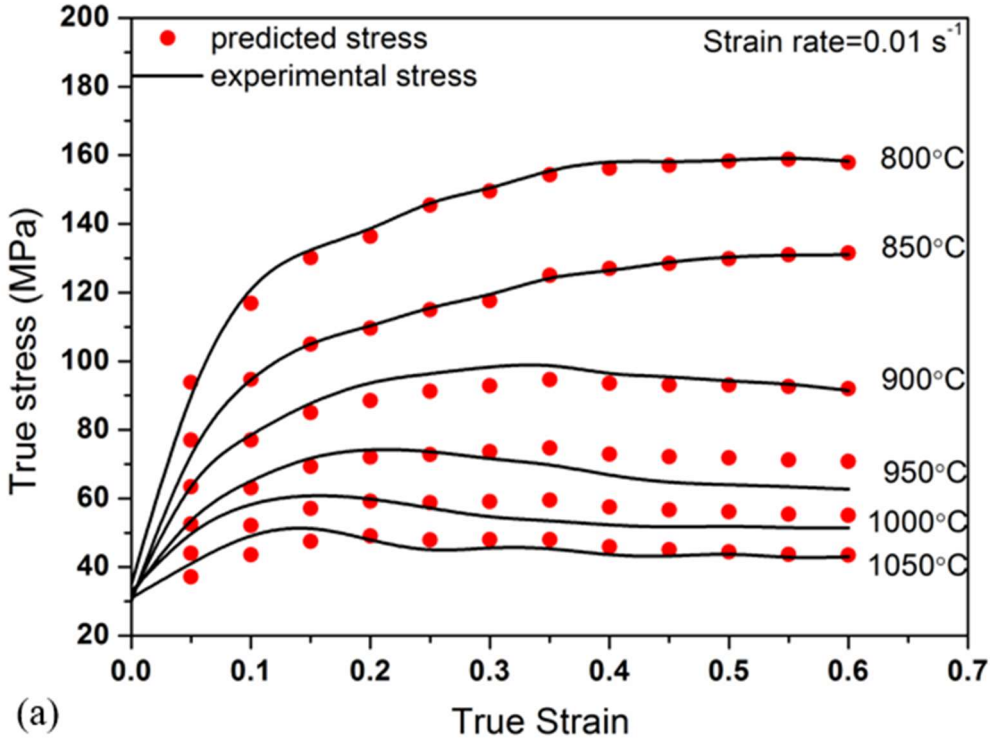
predicted stress
experimental stress
Strain rate=0.01 s-1
800°C
850°C
900°C
950°C
1000°C
1050°C
True stress (MPa)
True Strain
200
180
160
140
120
100
80
60
40
20
0.0
0.1
0.2
0.3
0.4
0.5
0.6
0.7

(a)

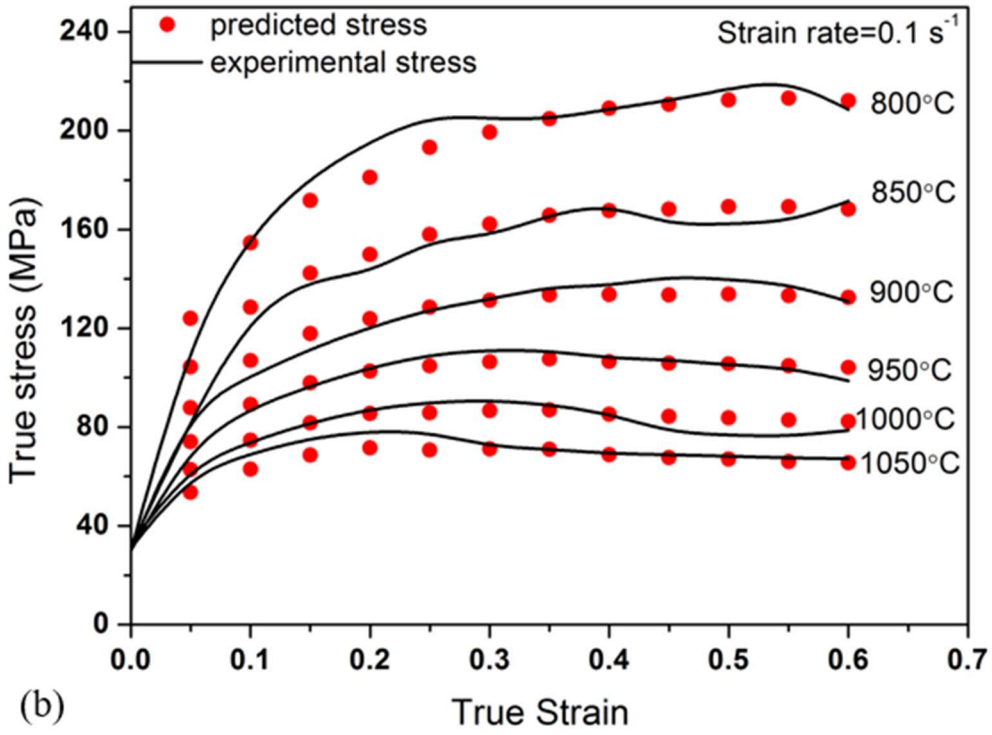
predicted stress
experimental stress
Strain rate=0.1 s-1
800°C
850°C
900°C
950°C
1000°C
1050°C
True stress (MPa)
True Strain
240
200
160
120
80
40
0
0.0
0.1
0.2
0.3
0.4
0.5
0.6
0.7

(b)

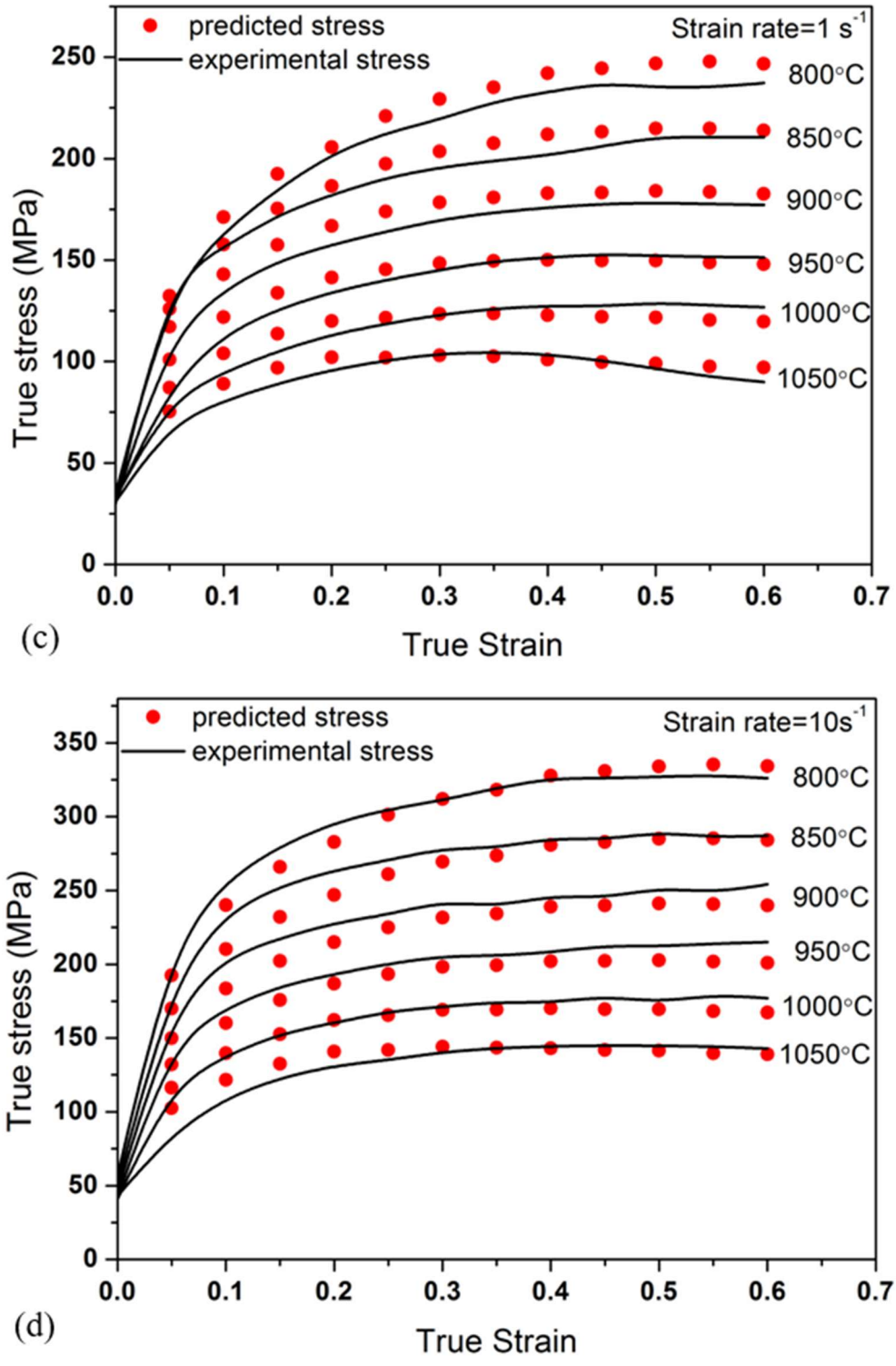

Fig. 5.10. Plots showing the experimental and predicted flow stress at strain rate; (a) 0.01 s^{-1}; (b) 0.1 s^{-1}; and (c) 1 s^{-1} and (d) 10 s^{-1} in the temperature domain 800–1050ºC.

5.4 Characterization of the hot deformed specimen

The simulated hot deformed specimens are cut along the center of compression axis into two semi-circular parts and then mounted by using epoxy resin for ease of metallography. The schematic diagram of the cut sample and area of interest for metallography is shown in Fig. 5.11. The central region is chosen for microscopy to avoid the effect of friction and dead and bulged zone in deformed specimen. The direction of the compression axis is kept horizontal during microscopy.

The micrographs of water-quenched specimens of LAMCS after austenitizing to 1100ºC for 2 min followed by hot compression at 800ºC and strain rates of 0.01, 0.1 and 10 s^{-1} for a total true strain of 0.7 are shown in Fig. 5.12. The dark phase present in the microstructure shows martensite and bright phase shows different amount of ferrite present in the microstructure. The amount of ferrite in the microstructure depends on the deformation temperature. At lower deformation temperature (inter critical region), the amount of ferrite present is more due to presence of some pro-eutectoid ferrite before the deformation. The ferrite formed during the deformation called the strain induced ferrite also contribute in increasing ferrite content in the microstructure. The micrographs of specimen deformed at 950ºC, 1000ºC and 1050ºC are shown in Fig. 5.13-Fig. 5.15 respectively. At the lower values of Zener-Hollomon parameter (i.e. at low strain rates and/or high temperatures) the nucleation and growth of new grains is increased [37] as shown in Fig. 5.12-Fig. 5.15.

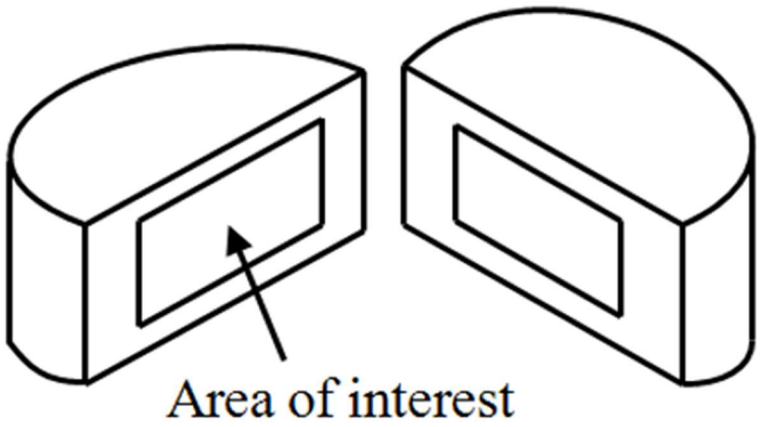

Fig. 5.11. Schematic diagram of deformed cut specimen showing area of interest for microstructural study where severe deformation takes place.

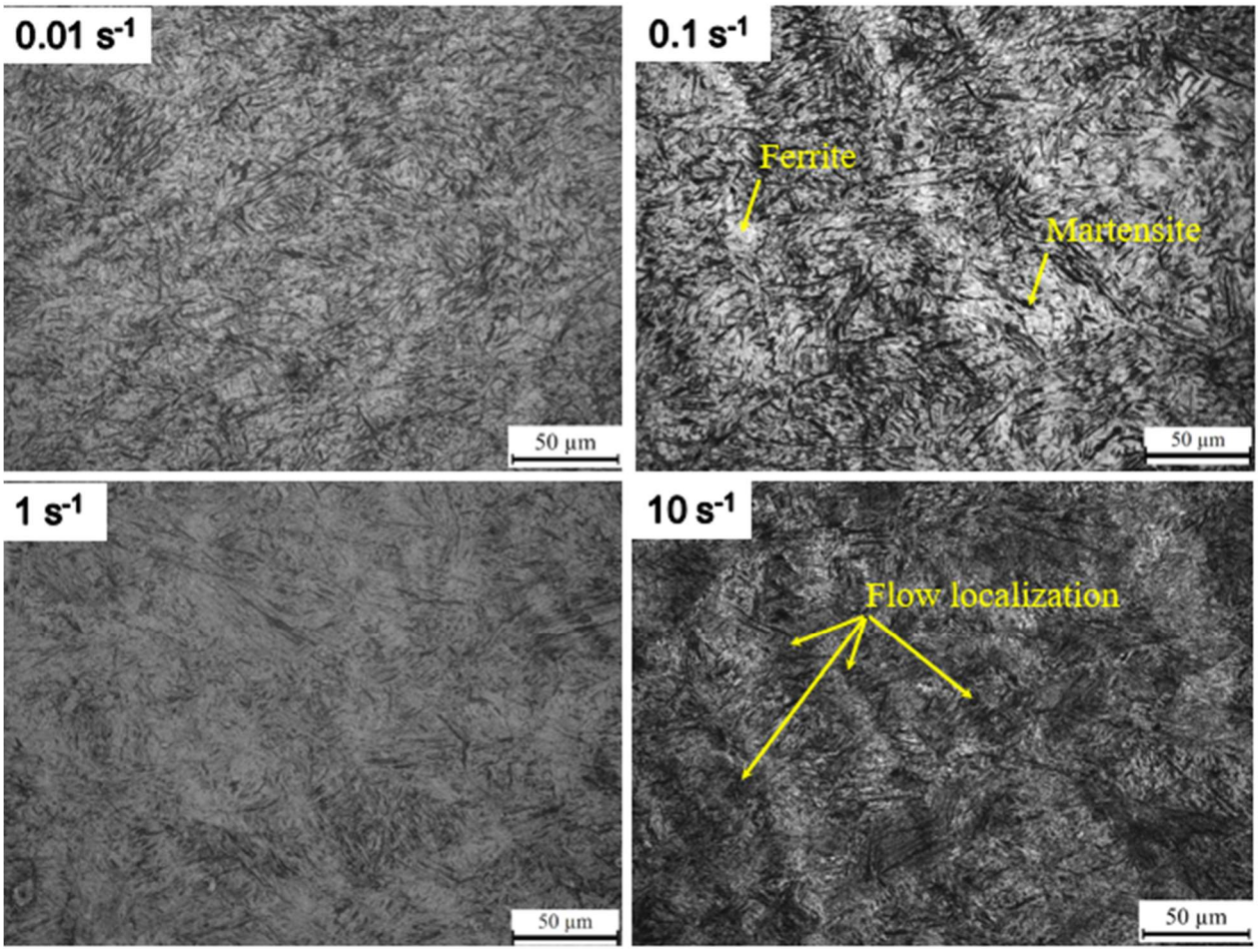

Fig. 5.12. Optical micrographs of LAMCS specimens after deformed at 800ºC. The axis of compression is horizontal.

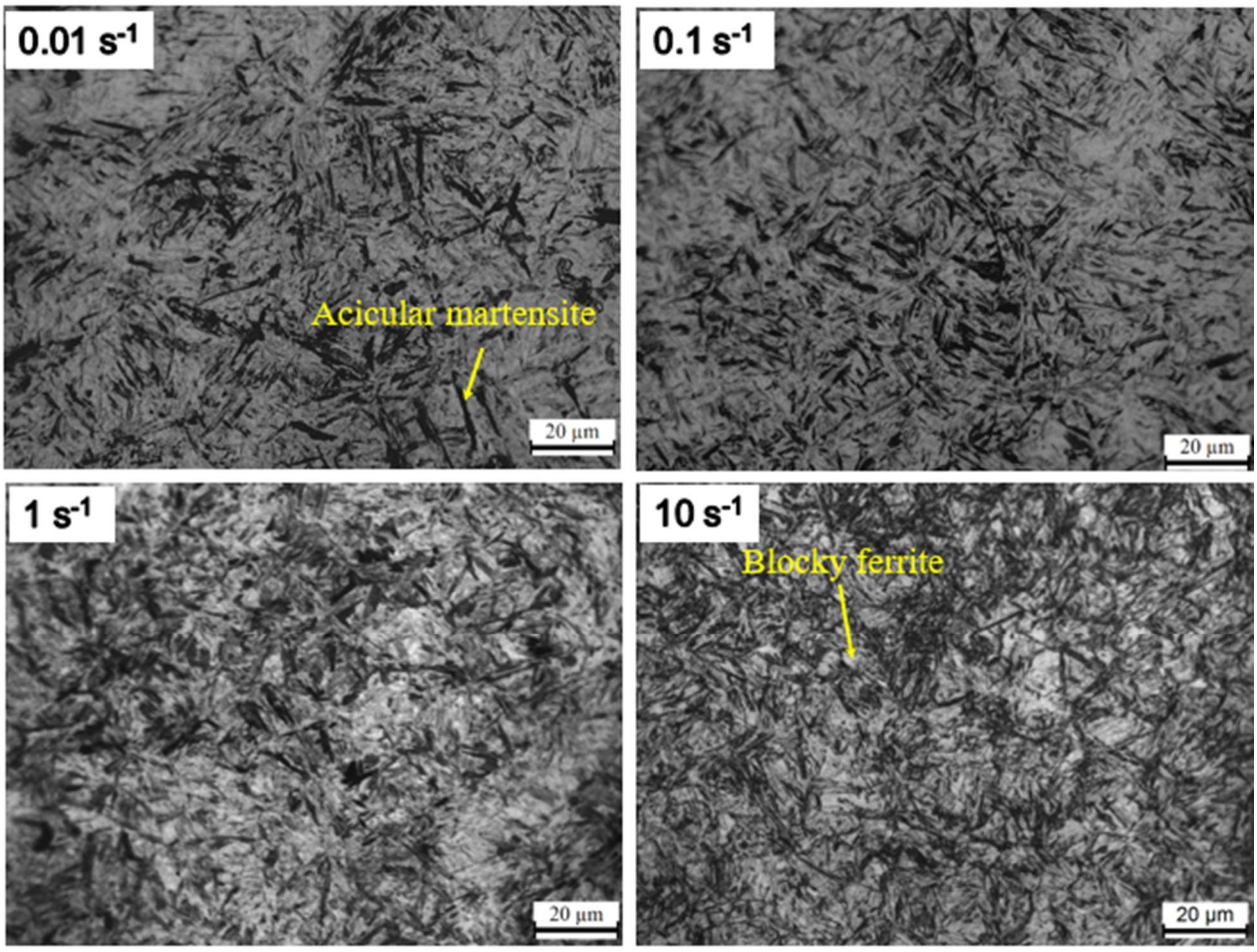

Fig. 5.13. Optical micrographs of LAMCS specimens after deformed at 950ºC. The axis of compression is horizontal.

The optical micrograph at deformation temperature 1000ºC with strain rate 0.1 s^{-1} shows ferrite in the shape of necklace due to large amount of DRX and DIFT at the prior austenite grain boundary (PAGB) (Fig. 5.14). Cracks have been observed along the blocky ferrite phase (Fig. 5.14). The SEM micrographs of specimens deformed at 800ºC and 0.01s^{-1} showing the pores observed and 950ºC and 0.01s^{-1} fine grains of ferrite and martensite shown by arrows (Fig. 5.16).

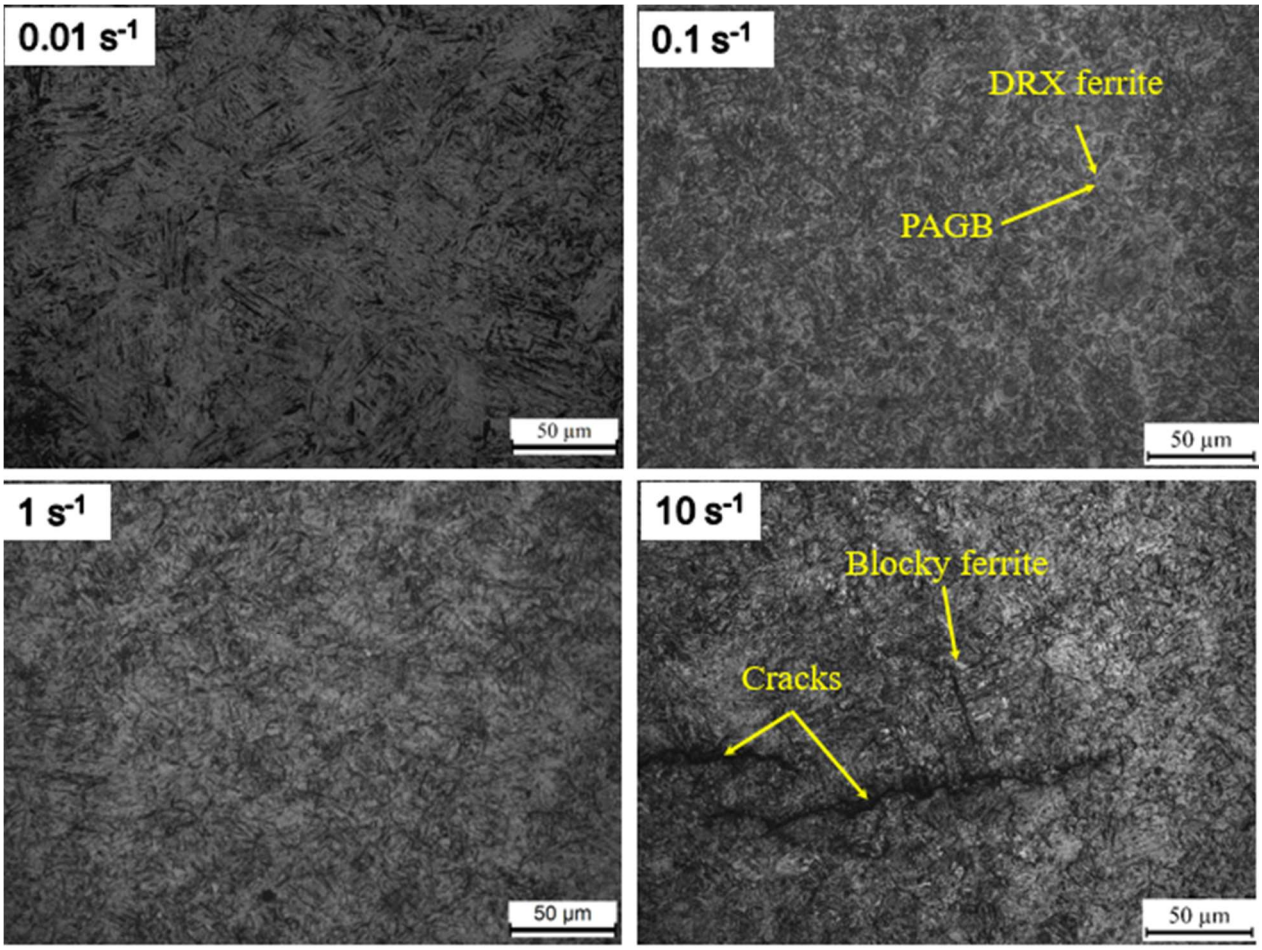

Fig. 5.14. Optical micrographs of LAMCS specimens after deformed at 1000ºC. The axis of compression is horizontal.

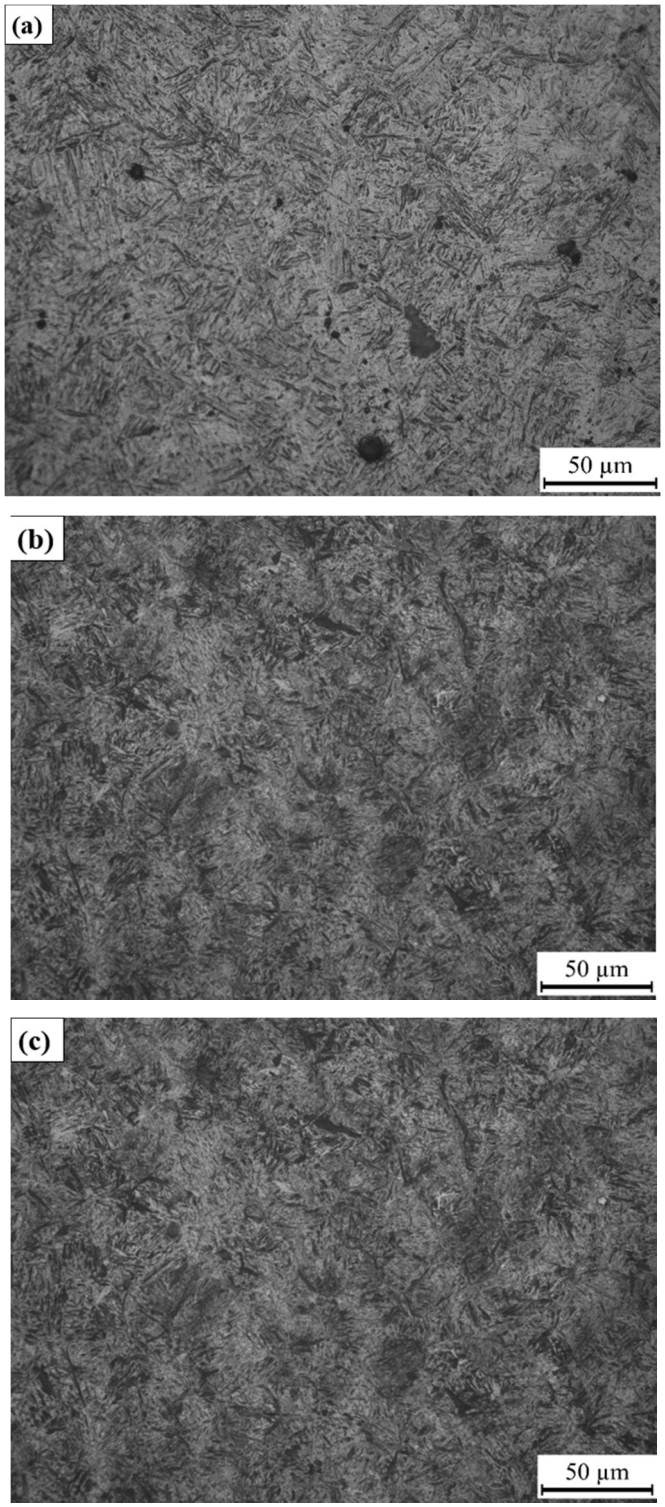

Fig. 5.15. Optical micrographs of LAMCS specimens after deformed at 1050ºC and strain rates of (a) 0.01 s^{-1}, (b) 0.1 s^{-1} and (c) 10 s^{-1}. The axis of compression is horizontal.

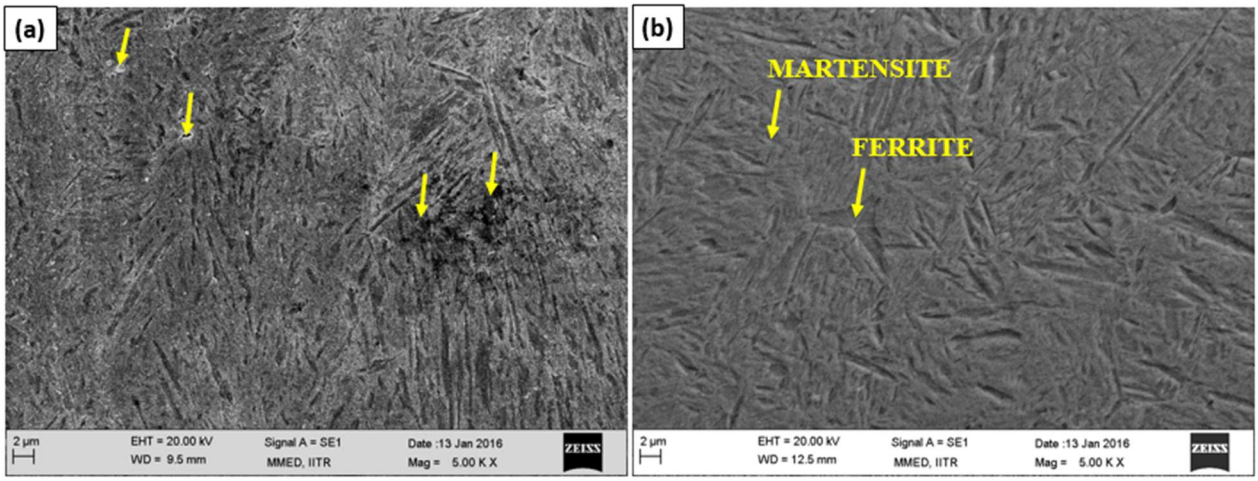

Fig. 5.16. SEM micrographs of steel specimen after hot compression at (a) 800ºC, 0.01s^{-1} (b) 950ºC, 0.01 s^{-1}. Pores are observed (shown by arrows).

5.5 Processing maps

To avoid accumulation of internal energy, the processing maps are plotted for strains after the strain hardening [38]. The processing maps of low alloy medium carbon steel based on strain rate sensitivity, dynamic materials model and modified dynamic materials model for true strain of 0.3 and 0.6 are shown in Fig. 5.17. The strain rate sensitivity (m) calculated by using Eq. (4.3) for true strain of 0.3 and 0.6 and was plotted on axes of temperature and logarithmic of strain rate to obtain strain rate sensitivity maps (Fig. 5.17 a & b). The maps have positive values of 'm' for the entire range of tests i.e. there is no instability predicted when power input equals power dissipation (D=P). High values of 'm' observed at high temperature for low and high strain rates. The value of strain rate sensitivity decreases as the value of strain rate increases. The higher values domains of 'm' at 0.3 strain shrinks with increase in strain to 0.6.

The power dissipation efficiency (η_{Prasad}) based on DMM (Eq. 4.5) and instability parameter (ξ) (Eq. 4.9) are plotted on axes of temperature and ln(strain rate) and superimposed to obtain the processing maps at 0.3 and 0.6 strain (Fig. 5.17 c & d). The iso-efficiency contour lines of DMM follows the same trend as the strain rate sensitivity contour lines. It can be observed that there exists following three domains in DMM based maps:

1. A lower efficiency zone in the temperature range of 800-900ºC and strain rate range of 0.01-3 s^{-1} with maximum efficiency of 24%.
2. A peak zone between 875-1050ºC and strain rate ranging from 0.01-3 s^{-1} having efficiency not less than 27%.

3. Another peak zone in the temperature range of 1025-1050ºC and strain rate ranging from 3-10 s^{-1} having also efficiency not less than 30%.

Similarly, Fig. 5.17 e & f show processing maps based on modified DMM where the iso-efficiency contours of $\eta_{\text{Murty and Rao}}$ (Eq. 4.6) and instability parameter, k (shaded area) (Eq. 4.10) superimposed at strain of 0.3 and 0.6 respectively. The values of $\eta_{\text{Murty and Rao}}$ increased with strains and shift towards higher temperature. The processing maps based on power dissipation efficiency of Murty and Rao (Eq. 4.6) and instability parameter of Poletti et al. (Eq. 4.11) at strain of 0.3 and 0.6 are shown in Fig. 5.18 a & b respectively. The k instability predicts a larger instability domain as compared to ξ instability parameter. But the instability zone predicted by k_j is smaller than k and ξ.

The DRX of austenite takes place at low strain rates and high temperatures which can be correlated with higher value of power dissipation efficiency domain and the flow curves (Fig. 5.5). The flow stress increases to a peak followed by softening towards a steady state which is a typical behavior observed during DRX. Under the condition of low Z parameter, the strain rate sensitivity and power dissipation efficiency have moderate to high value, and the flow stability is predicted due to higher tendency of nucleation and growth of new grains.

In general, the values of m and η increase with increase in temperatures for almost all strain rates as given by processing maps of different models. At low strain rates, large values of m & η, and smaller apparent activation energy are observed, which are related to diffusion controlled processes resulting in better workability. At high temperatures diffusion process takes place which is related to the DRX of austenite. Flow softening arises locally during hot working at high strain rates due to adiabatic heating, which results in defects like formation of voids/pores in the specimen. This is confirmed by the micrograph of specimen deformed at deformation temperature 1000ºC with strain rate of 10 s^{-1} (Fig. 5.14). This damage in the specimen is due to the short time of deformation (at high strain rates) because of less restoration phenomena such as DRX and dynamic recovery. The low values of strain rate sensitivity parameter m, also support the less restoration of microstructure.

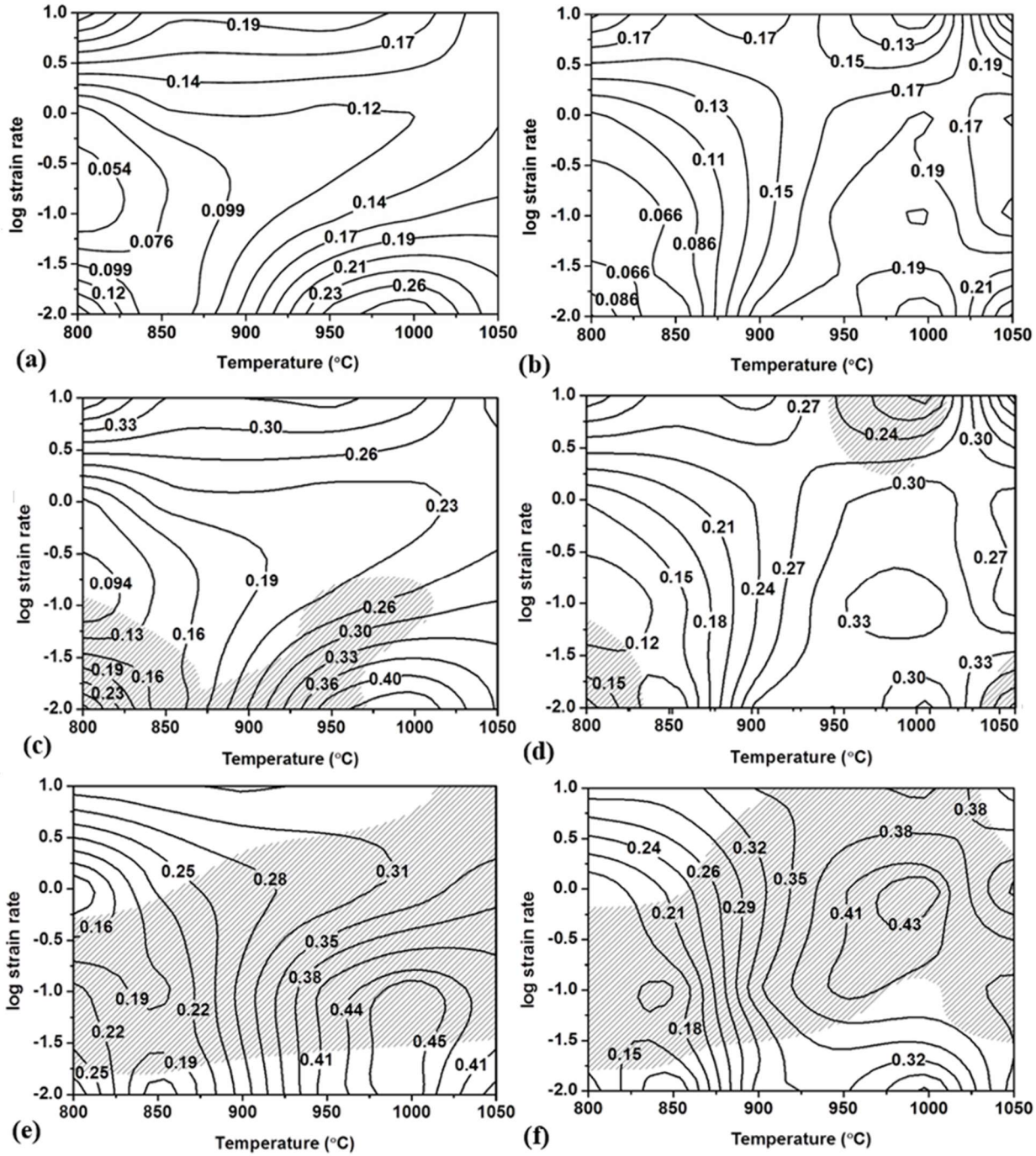

Fig. 5.17. Processing maps developed as a function of deformation temperature and strain rate for strain of 0.3 (left) and 0.6 (right). (a) & (b) strain rate sensitivity map; (c) & (d) DMM based maps; (e) & (f) modified DMM based maps.

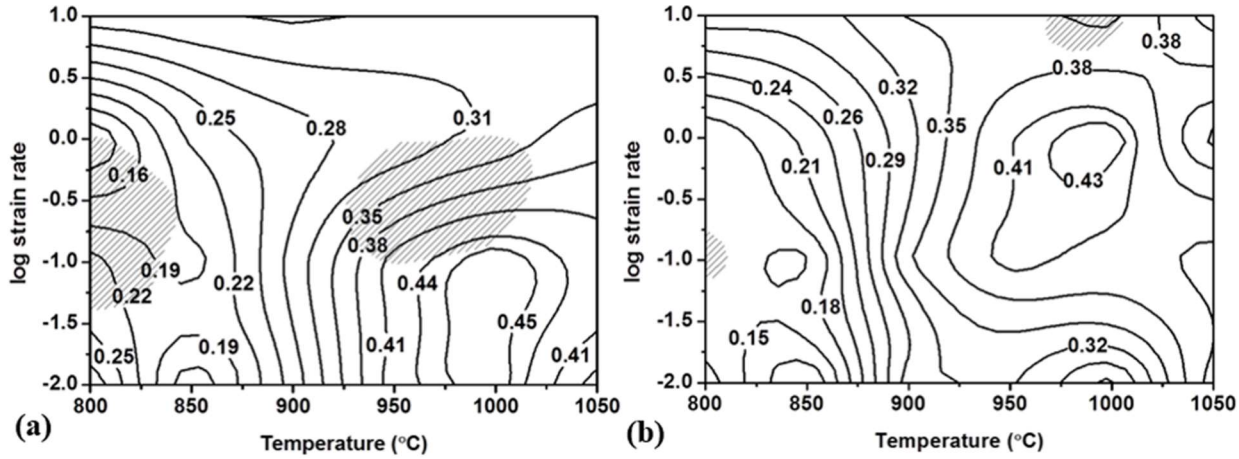

Fig. 5.18. Processing maps based on modified DMM efficiency and k_j instability criteria at strain of (a) 0.3 and (b) 0.6.

The optical micrographs of specimen deformed at 1000ºC and 0.1 s^{-1} showing the formation of necklace rings of ferrite at the grain boundary and prior austenite grain boundary is shown in Fig. 5.19. The SEM micrograph of specimen having lower 'm' values show initiation of cracks, pits and pores (Fig. 5.16a) but the specimen deformed at 950ºC have high value of 'm' and hence the micrograph shows fine recrystallized grains (Fig. 5.16b).

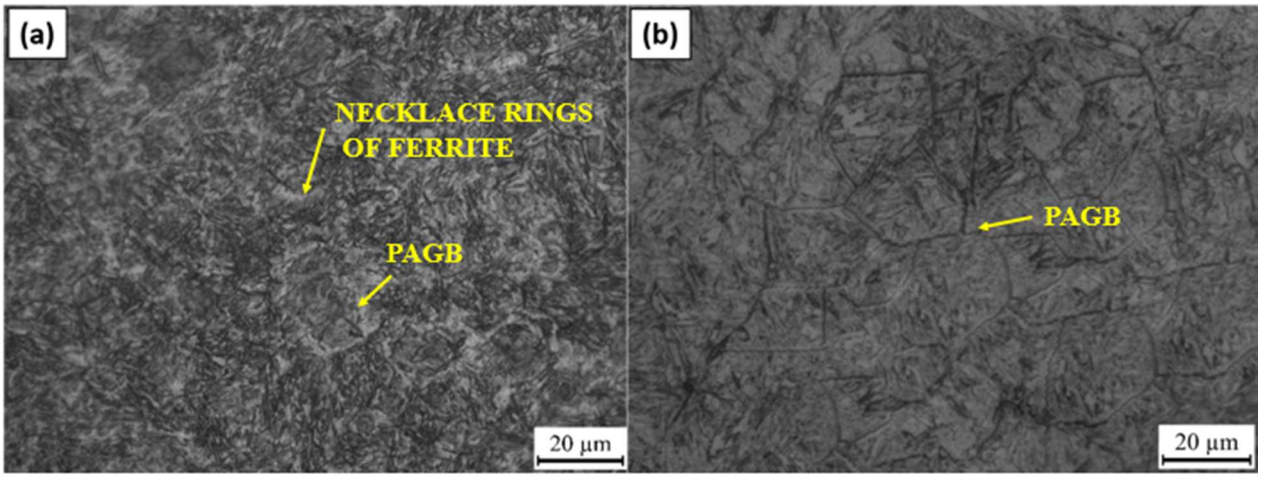

Fig. 5.19. Optical micrograph of deformed steel specimens at (a) 1000ºC and 0.1 s^{-1} showing ferrite necklace and (b) 1000ºC and 0.1 s^{-1} showing prior austenite grain boundary**.**

CHAPTER 6

SUMMARY

The hot compression behavior of low alloy medium carbon steel is studied under the strain rate range of 0.01-10 s^{-1} and temperature range of 800ºC -1050ºC. Modeling of flow behavior and prediction of flow stress are done using constitutive equation analysis. Processing maps are developed based on DMM, modified DMM and modified DMM with Poletti instability criteria. After proper study and observation of the obtained results, following conclusions are drawn from this work.

1. The values of strain rate sensitivity (m) and power dissipation efficiency are maximum at low strain rates and moderate to high temperatures. This is due to the occurrence of DRX and DRV.
2. The experimental stresses were corrected for adiabatic heating which is substantial at higher strain rates.
3. Larger amount of softening and hence more DRX and DRV are observed where the value of Z-parameter is smaller.
4. The deformation mechanisms during hot compression are studied using constitutive equations analysis.
5. The value of stress exponent, n is 5.4 shows that the mechanism of hot deformation is dislocation glide controlled by dislocation climb.
6. The apparent activation energy of hot deformation calculated for studied steel using hyperbolic sine law is found to be 368 $kJmol^{-1}$ at true strain of 0.6.
7. All the material constants and deformation activation energy are calculated and polynomial fitted to obtain a mathematical expression as a function of true strain.
8. The predicted flow stress values are found in good agreement with the experimental stress. This verified the established constitutive relation.
9. The efficiency of power dissipation η and the instability domain vary with the increasing strain which can be clearly observed from processing maps.
10. Metallographic investigations show that the damage at high strain rates occurs by a combination of limited restoration of microstructure due to short deformation times and possible adiabatic heating.

11. Studied material typically demonstrate the DRX behavior with a single stress peak flowed by softening towards the steady state in wide range of temperatures and strain rates. However, at high temperature and low strain rates, curves display cyclic DRX behavior having multiple peaks.

CHAPTER 7
FUTURE SCOPE OF THE WORK

In the present work, the hot deformation behavior of low alloy medium carbon steel is studied on Gleeble® 3800 thermo-mechanical simulator. The tests were carried out in wide temperature and strain rate range where carbides are fully dissolved. In continuation of this study, the behavior of low alloy medium carbon steel can be further analyzed in wide range of temperature and strain rate for partial dissolution of carbides. The comparison of the domains of processing maps for both cases can clearly explain the effect of alloying elements. This study will be useful and important contribution for this type of materials. The safe domains of processing parameters from processing maps should be used for sound defect free products. The flow behavior modeling would be done considering the effect of work hardening, DRX and DRV.

REFERENCES

[1] Z. Yang, F. Zhang, C. Zheng, M. Zhang, B. Lv, and L. Qu: Study on hot deformation behaviour and processing maps of low carbon bainitic steel, *Mater. Des.*, 2015, vol. 66, pp. 258–266.

[2] Y. V. R. K. Prasad, S.Venugopal, S.L. Mannan: Instability map for cold and warm working of as-cast 304 stainless steel, *J. Mater. Process. Technol.*, 1997, vol. 65, pp. 107–115.

[3] Y. V. R. K. Prasad and T. Seshacharyulu: Modelling of hot deformation for microstructural control, *Int. Mater. Rev.*, 1998, vol. 43, no. 6, pp. 243–258.

[4] S. V. S. N. Murty, S. Torizuka, and K. Nagai: Microstructural evolution during simple heavy warm compression of a low carbon steel: Development of a processing map, *Mater. Sci. Eng. A*, 2005, vol. 410–411, pp. 319–323.

[5] S. Venugopal and P. V. Sivaprasad: A Journey With Prasad's Processing Maps, *J. Mater. Eng. Perform.*, 2003, vol. 12, no. 6, pp. 674–686.

[6] Y. V. R. K. Prasad, H. L. Gegel, S. M. Doraivelu, J. C. Malas, and J. T. Morgan: Modeling of dynamic material behavior in hot deformation: Forging of Ti-6242, *Metall. Trans. A*, 1984, vol. 15, no. 10, pp. 1883–1892.

[7] S. Narayana Murty: On the hot working characteristics of 6061Al–SiC and 6061–Al_2O_3 particulate reinforced metal matrix composites, *Compos. Sci. Technol.*, 2003, vol. 63, no. 1, pp. 119–135.

[8] C. Poletti, J. Six, M. Hochegger, H. P. Degischer, and S. Ilie: Hot Deformation Behaviour of Low Alloy Steel, *steel Res. Int.*, 2011, vol. 82, no. 6, pp. 710–718.

[9] S. Venugopal, P. V. Sivaprasad, M. Vasudevan, S. L. Mannan, S. K. Jha, P. Pandey, and Y. V. R. K. Prasad: Validation of processing maps for 304L stainless steel using hot forging, rolling and extrusion, *J. Mater. Process. Technol.*, 1996, vol. 59, no. 4, pp. 343–350.

[10] M. Meysami and S. A. A. A. Mousavi: Study on the behavior of medium carbon vanadium microalloyed steel by hot compression test, *Mater. Sci. Eng. A*, 2011, vol. 528, no. 7–8, pp. 3049–3055.

[11] C. M. Sellars and W. J. M. Tegart: Hot Workability, *Int. Metall. Rev.*, 1972, vol. 17, pp. 1–24.

[12] J. Zhang, H. C. Kwon, H. Y. Kim, S. M. Byon, H. D. Park, and Y. T. Im: Micro-cracking of low carbon steel in hot-forming processes, *J. Mater. Process. Technol.*, 2005, vol. 162–163, pp. 447–453.

[13] H. Rastegari, A. Kermanpur, A. Najafizadeh, D. Porter, and M. Somani: Warm deformation processing maps for the plain eutectoid steels, *J. Alloys Compd.*, 2015, vol. 626, pp. 136–144.

[14] S. K. Rajput, M. Dikovits, G. P. Chaudhari, C. Poletti, F. Warchomicka, V. Pancholi, and S. K. Nath: Physical simulation of hot deformation and microstructural evolution of AISI 1016 steel using processing maps, *Mater. Sci. Eng. A*, 2013, vol. 587, pp. 291–300.

[15] Y. V. R. K. Prasad: Processing Maps: A Status Report, *J. Mater. Eng. Perform.*, 2003, vol. 12, no. 6, pp. 638–645.

[16] K. P. Rao and Y. K. D. V. Prasad: Neural network approach to flow stress evaluation in hot deformation, *J. Mater. Process. Technol.*, 1995, vol. 53, no. 3–4, pp. 552–566.

[17] A. Al Omar, J. M. Cabrera, and J. M. Prado: Characterization of the hot deformation in a microalloyed medium carbon steel using processing maps, *Scr. Mater.*, 1996, vol. 34, no. 8, pp. 1303–1308.

[18] Y. C. Lin, M. S. Chen, and J. Zhong: Microstructural evolution in 42CrMo steel during compression at elevated temperatures, *Mater. Lett.*, 2008, vol. 62, no. 14, pp. 2132–2135.

[19] Y. C. Lin, M. S. Chen, and J. Zhong: Constitutive modeling for elevated temperature flow behavior of 42CrMo steel, *Comput. Mater. Sci.*, 2008, vol. 42, no. 3, pp. 470–477.

[20] H. Zhao, G. Liu, and L. Xu: Rate-controlling mechanisms of hot deformation in a medium carbon vanadium microalloy steel, *Mater. Sci. Eng. A*, 2013, vol. 559, pp. 262–267.

[21] M. F. Ashby: A first report on deformation-mechanism maps, *Acta Metall.*, 1972, vol. 20, no. 7, pp. 887–897.

[22] G. Saada: Cross-slip and work hardening of f.c.c. crystals, *Mater. Sci. Eng. A*, 1991, vol. 137, pp. 177–183.

[23] U. F. Kocks: Laws for Work-Hardening and Low-Temperature Creep, *J. Eng. Mater.*

Technol., 1976, vol. 98, no. 1, pp. 76–85.

[24] H. J. McQueen and J. J. Jonas: Hot Workability Testing Techniques, in *Metal Forming: Interrelation Between Theory and Practice*, Springer, US, 1970, pp. 393–427.

[25] J. J. Jonas, C. M. Sellars, and W. J. M. Tegart: Strength and structure under hot-working conditions, *Metall. Rev.*, 1969, vol. 14, no. 1, pp. 1–24.

[26] R. Raj: Development of a processing map for use in warm-forming and hot-forming processes., *Metall. Trans. A, Phys. Metall. Mater. Sci.*, 1981, vol. 12 A, pp. 1089–1097.

[27] Porter D A, Easterling K E, Sherif Mohamed: Diffusional Transformations in Solids, in *Phase Transformations in metals and alloys*, 3rd ed., CRC Press, 1992, pp. 250–364.

[28] H. Ziegler: Progress in solid mechanics, John Wiley and Sons, New York, 1963, p. 93.

[29] S. V. S. N. Murty and B. N. Rao: Ziegler 's criterion on the instability regions in processing maps, *J. Mater. Sci. Lett.*, 1998, vol. 17, no. 14, pp. 1203–1205.

[30] K. K. Saxena, S. Sonkar, V. Pancholi, G. P. Chaudhari, D. Srivastava, G. K. Dey, S. K. Jha, and N. Saibaba: Hot deformation behavior of Zr-2.5Nb alloy: A comparative study using different materials models, *J. Alloys Compd.*, 2016, vol. 662, pp. 94–101.

[31] T. Sakai, A. Belyakov, R. Kaibyshev, H. Miura, and J. J. Jonas: Dynamic and post-dynamic recrystallization under hot, cold and severe plastic deformation conditions, *Prog. Mater. Sci.*, 2014, vol. 60, no. 1, pp. 130–207.

[32] Norman. E. Dowling: Mechanical Behaviour of Materials, in *Engineering Methods for Deformation, Fracture and Fatigue*, 4th edition, Pearsons Prentice Hall, London, 2013, pp. 1-936.

[33] Y. C. Lin, M. S. Chen, and J. Zhong: Effect of temperature and strain rate on the compressive deformation behavior of 42CrMo steel, *J. Mater. Process. Technol.*, 2008, vol. 205, no. 1–3, pp. 308–315.

[34] C. Zhang, L. Zhang, W. Shen, C. Liu, Y. Xia, and R. Li: Study on constitutive modeling and processing maps for hot deformation of medium carbon Cr–Ni–Mo alloyed steel, *Mater. Des.*, 2016, vol. 90, pp. 804–814.

[35] S. Sajadifar, G. Yapici, M. Ketabchi, and B. Bemanizadeh: High Temperature Deformation Behavior of 4340 Steel: Activation Energy Calculation and Modeling of Flow Response, *J. Iron Steel Res. Int.*, 2013, vol. 20, no. 12, pp. 133–139.

[36] D. Samantaray, S. Mandal, and A. K. Bhaduri: Constitutive analysis to predict high-temperature flow stress in modified 9Cr–1Mo (P91) steel, *Mater. Des.*, 2010, vol. 31, no. 2, pp. 981–984.

[37] S. M. Abbasi and A. Momeni: Hot working behavior of Fe–29Ni–17Co analyzed by mechanical testing and processing map, *Mater. Sci. Eng. A*, 2012, vol. 552, pp. 330–335.

[38] C. Poletti, H. Dieringa, and F. Warchomicka: Local deformation and processing maps of as-cast AZ31 alloy, *Mater. Sci. Eng. A*, 2009, vol. 516, no. 1–2, pp. 138–147.

LIST OF PUBLICATIONS

International Journal

1. **Niranjan Kumar,** Sanjeev Kumar, S.K. Rajput and S. K. Nath. "**Modeling of flow stress and prediction of workability by processing map for hot compression of 43CrNi steel**", Journal of Materials Processing technology (Under Review from 27th February 2016).

Conference

1. **Niranjan Kumar,** Sanjeev Kumar, and S. K. Nath. "Determination of Zener-Hollomon Parameter of a Low Alloy Medium Carbon Steel under Hot Compression Physical Simulation." Proceedings of the 4th International Conference on **Thermo mechanical Simulation and Processing of Steels** (SimPro'16), 10-12 February 2016, Ranchi, India, pp. 346-352.